Ross GW, Abbott RD, Petrovitch H, Morens DM, Grandinetti A, Tung KH, Tanner CM, Masaki KH, Blanchette PL, Curb JD, Popper JS, White LR. 2000. Association of coffee and caffeine intake with the risk of Parkinson disease. JAMA 283(20):2674–2679.

Schwarzschild MA, Chen JF, Ascherio A. 2002. Caffeinated clues and the promise of adenosine $A_{2A}$ antagonists in PD. Neurology 58(8):1154–1160.

Svenningsson P, Hall H, Sedvall G, Fredholm BB. 1997. Distribution of adenosine receptors in the postmortem human brain: An extended autoradiographic study. Synapse 27(4):322–335.

Todde S, Moresco RM, Simonelli P, Baraldi PG, Cacciari B, Spalluto G, Varani K, Monopoli A, Matarrese M, Carpinelli A, Magni F, Kienle MG, Fazio F. 2000. Design, radiosynthesis, and biodistribution of a new potent and selective ligand for in vivo imaging of the adenosine $A_{2A}$ receptor system using positron emission tomography. J Med Chem 43(23):4359–4362.

Wang WF, Ishiwata K, Nonaka H, Ishii S, Kiyosawa M, Shimada J, Suzuki F, Senda M. 2000. Carbon-11-labeled KF21213: A highly selective ligand for mapping CNS adenosine $A_{2A}$ receptors with positron emission tomography. Nucl Med Biol 27(6):541–546.

# Mapping of human cerebral sigma$_1$ receptors using positron emission tomography and [11C]SA4503

Muneyuki Sakata,[a] Yuichi Kimura,[b,*] Mika Naganawa,[b,c] Keiichi Oda,[b] Kenji Ishii,[b] Kunihiro Chihara,[a] and Kiichi Ishiwata[b]

[a]*Graduate School of Information Science, Nara Institute of Science and Technology, Japan*
[b]*Positron Medical Center, Tokyo Metropolitan Institute of Gerontology, 1-1, Naka, Itabashi, Tokyo 173-0022, Japan*
[c]*Japan Society for the Promotion of Science, Japan*

The objective of this study was to establish the kinetic analysis for mapping sigma$_1$ receptors ($\sigma$1Rs) in the human brain by positron emission tomography (PET) with [11C]SA4503. The $\sigma$1Rs are considered to be involved in various neurological and psychiatric diseases. [11C]SA4503 is a recently developed radioligand with high and selective affinity for $\sigma$1Rs, and we have first applied it to clinical studies. Nine healthy male subjects each underwent a dynamic 90-min PET scan after injection of [11C]SA4503. In addition to the baseline measurement, three of the nine subjects underwent a second [11C] SA4503-PET after partial blockade of $\sigma$1Rs by oral administration of haloperidol, a sigma receptor antagonist. Full kinetic analysis using two times nonlinear estimations was applied for fitting a two-tissue three-compartment model to determine the binding potential (BP) and total distribution volume (tDV) of [11C]SA4503. Graphical analysis with a Logan plot was also applied for estimations of tDV. The regional distribution patterns of BP and tDV in 11 regions were compatible with those of previously reported $\sigma$1Rs *in vitro*. The reduced binding sites of $\sigma$1Rs by haloperidol were appropriately evaluated. The tDVs derived from the two methods matched each other well. The Logan plot offered images of the tDV, which reflected $\sigma$1R densities, and the tDV in the images decreased after haloperidol loading. Moreover, comparison of BPs calculated with and without metabolite correction for plasma input function indicated that the metabolite correction could be omitted. We concluded that this method enables the quantitative analysis of $\sigma$1Rs in the human brain.
© 2006 Elsevier Inc. All rights reserved.

## Introduction

Sigma receptors are classified into sigma$_1$ and sigma$_2$ subtypes. The former was cloned but the latter was not. These subtypes display a different tissue distribution and a distinct physiological and pharmacological profile in the central and peripheral nervous system. The receptors are related to neurological and psychiatric neurophysiologies (Su, 1993; Su and Hayashi, 2003; Junien and Leonard, 1989). In the central nervous system (CNS), the sigma$_1$ receptors ($\sigma$1Rs) might play a role as a modulator of signal transduction in neurotransmitter systems such as N-methyl-D-aspartate (NMDA) receptors. Peripherally, the two sigma receptor subtypes are also expressed on tumor cells, where they could be of prognostic relevance. The discovery of new specific sigma receptor ligands demonstrated that sigma receptors are novel targets for the therapeutic treatment of neuropsychiatric diseases (schizophrenia, depression, and cognition) and brain ischemia and also for treating cancer (Hashimoto and Ishiwata, 2006). In several studies on postmortem brains taken from individuals with schizophrenia and Alzheimer's disease, these brains have altered densities of $\sigma$1Rs (Weissman et al., 1991; Shibuya et al., 1992; Jansen et al., 1993; Helmeste et al., 1996). Thus, the sigma receptors in the CNS are an interesting target for molecular imaging with positron emission tomography (PET) and single photon emission computed tomography (SPECT). These imaging techniques targeting sigma receptors have also provided the opportunity for the development of new drugs, evaluation of the therapeutic effects of the drugs, and better informed decisions about appropriate dosage of drugs in relation to neurological and psychiatric disorders. So far, many radioligands have been proposed for the *in vivo* imaging of sigma receptors in the brain. Preliminary clinical application of the two PET candidates, 1-(3,4-dimethoxyphenthyl)-4-(3-phenylpropyl)-piperazine hydrochloride ([11C]SA4503; Fig. 1) and 1-(3-[18F] fluoropropyl)-4-(4-cyanophenoxymethyl)piperidine ([18F]FPS), and the clinical application of tumor imaging by SPECT were reviewed (Hashimoto and Ishiwata, 2006). Recently, [11C]SA4503-PET was applied to patients with Parkinson's disease (Mishina et al., 2005). More recently, Mach et al. (2005) visualized $\sigma$1Rs in monkey brains by PET with N-[18F]4'-fluorobenzylpiperidin-4yl-(2-fluorophenyl) acetamide ([18F]FBFPA) (2005), and Stone et al. (2006) succeeded the mapping $\sigma$1Rs in the human brain by SPECT

* Corresponding author. Fax: +81 3 3964 2188.
  *E-mail address:* ukimura@ieee.org (Y. Kimura).
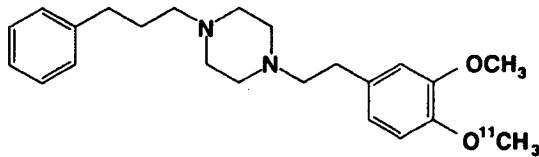  Available online on ScienceDirect (www.sciencedirect.com).

Fig. 1. Chemical structure of [$^{11}$C]SA4503.

with 1-(trans-[$^{123}$I]iodopropen-2-yl)-4-[(4-cyanophenoxy)methyl] piperidine ([$^{123}$I]TPCNE).

SA4503 has been originally developed by Matsuno and co-workers and has high affinity (IC$_{50}$, 17.4 nM) and high selectivity (sigma$_1$/sigma$_2$, 103) for σ1Rs but low affinity for other receptors such as dopamine D$_2$ and histamine H$_1$ receptors (Matsuno et al., 1996; Matsuno and Mita, 1998). Kawamura et al. (2000a, b) demonstrated that the carbon-11 labeled SA4503 selectively bound in vivo to σ1Rs, but not to sigma$_2$ and other receptors. Further in vivo studies on rodents (Ishiwata et al., 2003), cats (Kawamura et al., 2000a) and monkeys (Ishiwata et al., 2001; Kawamura et al., 2003) have demonstrated that [$^{11}$C]SA4503-PET has the potential to map σ1Rs. In addition, the application of [$^{11}$C]SA4503-PET to patients with Parkinson's disease or Alzheimer's diseases revealed the regional alteration of σ1Rs in the brains of these subjects (Mishina et al., 2005; Hashimoto and Ishiwata, 2006).

Thus, our aim in this study was to establish a quantitative way of evaluating the binding of [$^{11}$C]SA4503 to σ1Rs in the human brain. We performed [$^{11}$C]SA4503-PET in healthy young adults. First, a method for full compartment analysis was investigated, and a baseline measurement was established. Then, the method was validated for [$^{11}$C]SA4503-PET under haloperidol challenge, where the available binding sites of σ1Rs in the brain were artificially changed by partial blockade using haloperidol, a typical and nonselective sigma receptor antagonist (Ishiwata et al., 2001, 2003). Furthermore, a graphical analysis using the Logan plot (Logan et al., 1990) was applied to the data to visualize a spatial distribution of the binding parameter of [$^{11}$C]SA4503 with σ1Rs. The Logan plot is a faster and more stable method for estimation of total distribution volume (tDV) of the PET radioligand in comparison with a compartment model analysis based on a nonlinear estimation (NLE). The possibility of omitting metabolite correction for the plasma input function was also studied to conveniently apply [$^{11}$C]SA4503-PET to various clinical studies.

## Materials and methods

### Subjects and study protocol

Nine normal male volunteers with a mean age of 28±4 years were recruited. They had no neurological disorders and no abnormalities in MRIs of their brains. All subjects underwent a PET scan with [$^{11}$C]SA4503 as the baseline. After a 2–6 weeks interval, three of the nine subjects were given 3 mg of haloperidol orally, and 18 h later a second [$^{11}$C]SA4503-PET was performed. Upon treatment with haloperidol, a nonselective sigma receptor antagonist, the σ1Rs in the brain were partially blocked (Ishiwata et al., 2001, 2003), and a reduced density of σ1Rs was apparently produced.

[$^{11}$C]SA4503 was prepared as previously described (Kawamura et al., 2000a,b). The injected doses (mean±standard deviation (SD)) and the specific activity were 587±177 MBq/

13.2±25.7 nmol and 57±11 TBq/mmol at the baseline condition ($n=9$), and 435±306 MBq/18.6±11.1 nmol and 21±26 TBq/mmol at the haloperidol loading condition ($n=3$).

The Ethics Committee of Tokyo Metropolitan Institute of Gerontology approved the study protocol, and informed consent was given by all subjects.

### PET data acquisition

The PET camera used was a SET-2400 (Shimadzu Co., Kyoto, Japan), which had an axial field-of-view of 20 cm, acquired 63 slices at a center-to-center interval of 3.125 mm and had a spatial resolution of 4.4 mm full width at half maximum (FWHM) and a Z-axis resolution of 6.5 mm FWHM (Fujiwara et al., 1997). The 5 min transmission data were acquired with a rotating [$^{68}$Ge]/[$^{68}$Ga] line source to correct for attenuation. Then, [$^{11}$C]SA4503 was injected intravenously into each subject and a 90 min dynamic scan in 2D mode (10 s×6 frames, 30 s×3 frames, 60 s×5 frames, 150 s×5 frames and 300 s×14 frames) was performed, with 27 arterial blood samplings at 10, 20, 30, 40, 50, 60, 70, 80, 90, 100, 110, 120, 135 and 150 s and 3, 5, 7.5, 10, 15, 20, 30, 40, 50, 60, 70, 80 and 90 min. Each blood volume sample was 1 mL. To analyze the labeled metabolites, 2 mL of additional blood was obtained at 3, 5, 10, 15, 20, 30, 40 and 60 min. The plasma obtained by centrifugation was weighed and the radioactivity was measured with a well-type gamma-counter (BSS-1; Shimadzu Co., Kyoto, Japan), the sensitivity of which was calibrated with the PET camera. Thus, the time activity curve in arterial plasma (pTAC) was calculated as becquerels per milliliter.

Metabolites of [$^{11}$C]SA4503 in the plasma sampled were analyzed by high-performance liquid chromatography (HPLC) in accordance with a previously described method (Kawamura et al., 2000b). Briefly, 0.8–0.9 mL plasma was treated with one third volume of acetonitrile containing 20% trichloroacetic acid. After centrifugation, the homogenate was divided into an acid-soluble supernatant and a precipitate. The latter was washed twice with 1.0 mL of acetonitrile containing 10% trichloroacetic acid. The supernatant was diluted with 50 mM sodium acetate (pH 4.5) until the concentration of acetonitrile was 40%. Most radioactivity (>95%) in the plasma was recovered in the acid-soluble supernatant. Then, the solution was analyzed by HPLC: column, Nova-pak C18 (8 mm×100 mm; Waters, Milford, MA); eluent, acetonitrile: 50 mM sodium acetate, pH 4.5 (4:6, v/v); flow rate, 2 mL/min; and radioactivity monitor, FLO-ONE/Beta A200 (Packard, Meriden, CT). The recovery of radioactivity in the HPLC analysis was essentially quantitative.

Metabolite correction was made to pTAC values in subsequent data analyses. For this correction, the empirical function proposed by Watabe et al. (2000), $1/(1+(\alpha t)^2)^\beta$, was fitted with the Nelder–Meads simplex algorithm (Nelder and Mead, 1965) using a least squares method with initial guesses of 0.1 for both $\alpha$ and $\beta$ (Kimura et al., 2004).

The dynamic image was reconstructed with a back-projection algorithm using a Butterworth filter with a cut-off frequency of 1.25 cycles/cm. The data were collected in a 128×128×63 matrix, and the voxel size was 2×2×3.125 mm. PET images were co-registered with MRI using the Automated Medical Images Registration (AMIR) program (Ardekani et al., 1995), and the regions of interest (ROIs) were located on the frontal, temporal, parietal, and occipital cortices, hippocampus, caudate, putamen, thalamus, anterior cingulated gyrus, cerebellar vermis

and cerebellar hemisphere. The sizes of the ROIs were between 1.5 mm$^3$ and 36.3 mm$^3$ (mean±SD=11.3±8.6 mm$^3$). Time activity curves in the tissues (tTACs) were calculated as becquerels per milliliter.

## Kinetic analysis

Based on the assumption that the nonspecific binding component is in equilibrium with a free compartment (Koeppe et al., 1991), a two-tissue three-compartment model was fitted on the tTAC. The composition and relation of the three compartments are shown in Fig. 2; $C_p$, $C_f$ and $C_b$ denote the concentration of radioligand in arterial plasma, free compartment and specifically bound compartment, respectively; $K_1$ and $k_2$ denote rate constants of delivery from plasma to brain tissue through the blood–brain barrier and a clearance from tissue to plasma; $k_3$ and $k_4$ are association and dissociation rate constants, respectively, between the free component and the specifically bound component.

The estimation process comprised two steps for stable estimations. In the first step, a delay between tTACs and pTAC was estimated with the rate parameters because it was more sensitive than other parameters. In the second step, after fixing the delay, all rate constants were estimated. Both steps were based on NLE and were implemented using the interior-reflective Newton method (Coleman and Branch, 1999). Blood volumes were fixed at 3%, and non-negative constraints for $K_1$, $k_2$, $k_3$ and $k_4$ were used. The SD derived from the tTAC of each ROI was used to realize stable estimation (Bard, 1974), and the evaluated values of each frame were weighted by 1/SD in the iterative calculations. Moreover, the first two frames of a PET scan after administration of [$^{11}$C]SA4503 were discarded before the estimation because of the small signal-to-noise ratios from slow injection of the tracer. Initial guesses were 0.4 for $K_1$, 0.2 for $k_2$, 0.3 for $k_3$ and 0.02 for $k_4$. In this study, the convergences of estimates were confirmed by additional estimations, i.e., the initial guesses of the estimation were set to the estimated results of the second step. Then, a distribution volume of the free compartment and a tDV were calculated as $K_1/k_2$ and $(K_1/k_2)(1+k_3/k_4)$, respectively, and a binding potential (BP) was computed as $k_3/k_4$ (Mintun et al., 1984). To investigate the possibility of omitting the metabolite correction for pTAC, BPs with and without metabolite-corrected pTACs were compared with each other.

Additionally, the Logan plot (Logan et al., 1990) was applied to the tTAC of each ROI and to the dynamic images. The time
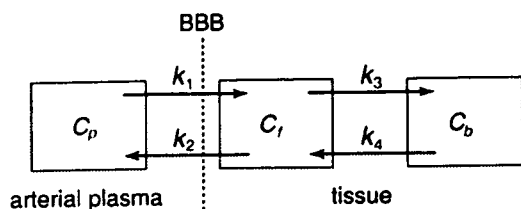


Fig. 3. Typical time–activity curve and the amount of intact [$^{11}$C]SA4503 in arterial plasma. Total radioactivity and metabolite corrected radioactivity are plotted in dashed and solid lines, respectively. The mean with standard deviation of the amount of intact [$^{11}$C]SA4503 is shown in an upper curve ($n$=12). At 60 min, 89% of administered [$^{11}$C]SA4503 remained in an intact form.

intervals, especially the starting time for the Logan plot, were examined.

## Results

### pTACs and tTACs

Time courses for the fraction of unchanged [$^{11}$C]SA4503 in plasma and pTACs with and without metabolite correction are shown in Fig. 3. Eighty-nine percent of the administered [$^{11}$C] SA4503 remained in an intact form 60 min after injection. Metabolism was not altered between the baseline and haloperidol loading: their ratios of an intact form (mean±SD) were 94.7±2.2% and 97.6±0.9%, respectively, 30 min postinjection. The plots in Fig. 4 describe typical tTACs in the parietal cortex, frontal cortex



Fig. 2. Two-tissue three-compartment model. $C_p$ is the compartment for arterial plasma, $C_f$ is the free compartment of tissue and $C_b$ is the specifically bound compartment of tissue. $K_1$ and $k_2$ are rate constants for the radioligand transfer between arterial plasma and brain tissue through the blood–brain barrier (BBB), and $k_3$ and $k_4$ are rate constants between free and specific binding components.
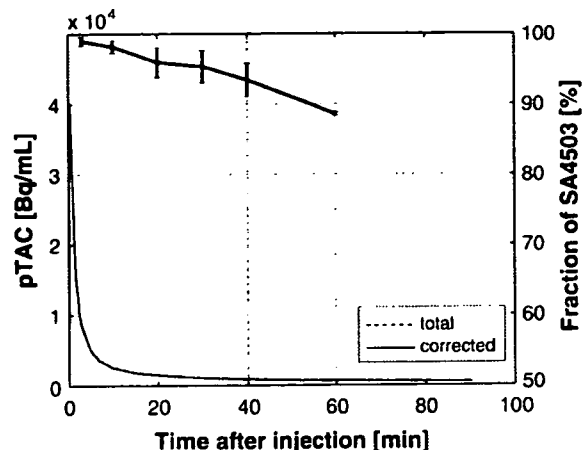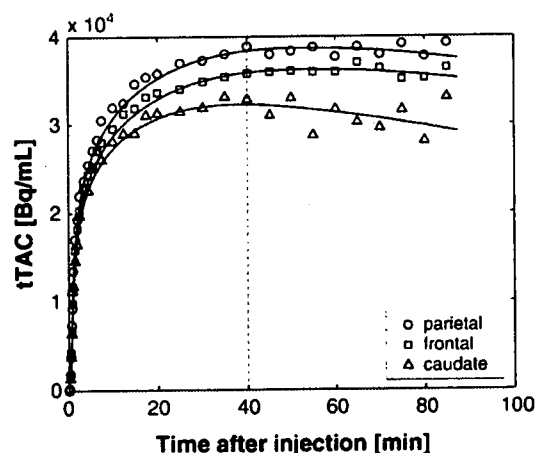


Fig. 4. Typical time–activity curves of the parietal cortex, frontal cortex and caudate in baseline conditions. The predicted curves, estimated by proposed nonlinear estimation algorithm, are superimposed on the time–activity curves.

*M. Sakata et al. / NeuroImage 35 (2007) 1–8*

Table 1
Estimated kinetic parameters (mean±SD, $n=9$) at baseline conditions in the brain using a nonlinear estimation algorithm

| | $K_1$ [mL/g/min] | $k_2$ [1/min] | $k_3$ [1/min] | $k_4$ [1/min] | Distribution volume of free compartment [mL/g] | Total distribution volume [mL/g] | Binding potential |
|---|---|---|---|---|---|---|---|
| Frontal cortex | 0.49±0.080 | 0.19±0.024 | 0.43±0.065 | 0.024±0.0044 | 2.6±0.60 | 49±8.0 | 19±4.5 |
| Temporal cortex | 0.43±0.065 | 0.20±0.029 | 0.47±0.084 | 0.021±0.0040 | 2.2±0.52 | 51±11.1 | 23±6.0 |
| Parietal cortex | 0.48±0.091 | 0.21±0.036 | 0.47±0.092 | 0.023±0.0047 | 2.4±0.61 | 49±7.1 | 21±8.4 |
| Occipital cortex | 0.53±0.085 | 0.20±0.004 | 0.41±0.056 | 0.023±0.0042 | 2.6±0.41 | 50±10.0 | 18±4.6 |
| Hippocampus | 0.43±0.074 | 0.25±0.094 | 0.46±0.113 | 0.018±0.0050 | 1.9±0.67 | 50±9.5 | 30±18.7 |
| Caudate | 0.52±0.103 | 0.20±0.014 | 0.42±0.076 | 0.028±0.0052 | 2.6±0.43 | 42±6.8 | 15±2.1 |
| Putamen | 0.56±0.105 | 0.20±0.025 | 0.44±0.068 | 0.027±0.0036 | 2.8±0.42 | 47±6.9 | 16±3.3 |
| Thalamus | 0.55±0.090 | 0.20±0.017 | 0.42±0.040 | 0.023±0.0035 | 2.8±0.32 | 53±8.6 | 19±3.4 |
| Anterior cingulated gyrus | 0.51±0.089 | 0.20±0.008 | 0.44±0.054 | 0.021±0.0023 | 2.5±0.39 | 56±9.6 | 22±4.2 |
| Cerebellar vermis | 0.50±0.052 | 0.20±0.009 | 0.49±0.063 | 0.020±0.0032 | 2.5±0.24 | 64±8.9 | 25±4.7 |
| Cerebellar hemisphere | 0.49±0.063 | 0.20±0.005 | 0.54±0.084 | 0.020±0.0024 | 2.4±0.29 | 70±11.4 | 28±5.7 |

and caudate in the baseline condition. The radioactivity gradually accumulated in tissues.

*Kinetics*

The results of curve-fitting are superimposed in Fig. 4. The time courses are described well with the compartment analysis. The estimated kinetic parameters in 11 regions of the brain using the NLE algorithm are summarized in Table 1. In the third estimation for the validation of the convergence, 94% of the estimates converged to within 10% of the results of the proposed two-step estimation, demonstrating the stability of the proposed estimation process. BPs and tDVs were significantly decreased after haloperidol loading in all regions investigated (Table 2).

Fig. 5 represents the influence of metabolite correction for pTAC on BP. Good agreement was observed between the two estimates ($y=0.87x+0.58$, $r^2=0.98$). The pTAC without metabolite correction caused an underestimation of 13% for the BPs, and no regional, subject-oriented, or pharmacological loading dependencies were found in the underestimation.

Table 2
The total distribution volumes and binding potentials (mean±SD, $n=3$) at baseline and haloperidol loading conditions in the brain tissues of three normal subjects using a nonlinear estimation algorithm

| | Total distribution volume [mL/g] | | Binding potential | |
|---|---|---|---|---|
| | Baseline | Loading | Baseline | Loading |
| Frontal cortex | 47±7.5 | 15±2.3* | 21±0.7 | 3.8±0.9* |
| Temporal cortex | 49±12.1 | 16±2.6** | 25±2.2 | 4.8±1.0* |
| Parietal cortex | 51±6.8 | 15±3.0* | 29±10.4 | 3.9±1.4 |
| Occipital cortex | 52±12.0 | 16±2.2** | 21±3.9 | 4.2±1.6** |
| Hippocampus | 47±5.1 | 16±2.6* | 34±12.7 | 6.9±2.5** |
| Caudate | 37±3.0 | 14±1.5* | 15±1.2 | 3.0±0.6* |
| Putamen | 46±7.8 | 16±1.4** | 17±3.6 | 3.6±0.3** |
| Thalamus | 53±8.2 | 17±1.7** | 21±1.9 | 4.9±1.2* |
| Anterior cingulated gyrus | 59±13.4 | 16±2.9** | 25±2.6 | 4.3±1.3* |
| Cerebellar vermis | 65±7.6 | 18±1.8* | 27±2.8 | 5.6±1.4* |
| Cerebellar hemisphere | 69±7.1 | 20±2.7* | 29±1.3 | 5.5±1.2* |

The total distribution volumes and binding potentials decreased significantly after haloperidol loading: *$p<0.01$ and **$p<0.05$.

*Logan plot analysis*

Typical Logan plots are shown in Fig. 6. Frames from 30 min to 90 min after administration were used for Logan plot analysis, and good linear relationships were observed in the plots of baseline and haloperidol loading conditions for most regions investigated. The linearity tended to worsen for small regions, such as the cerebellar vermis, and these tDVs were underestimated for the regions. Changes in the estimated tDVs in accordance with the starting time of the data used for the estimations are shown in Fig. 7. The starting time affected the estimated tDVs. However, the effects were less than 10% when the starting time was changed from 20 min to 40 min.

A comparison between the tDVs estimated by NLE and those estimated by Logan plot analysis is shown in Fig. 8. The data obtained from all regions of all scans except for those of the cerebellar vermis have been plotted. There is good coincidence
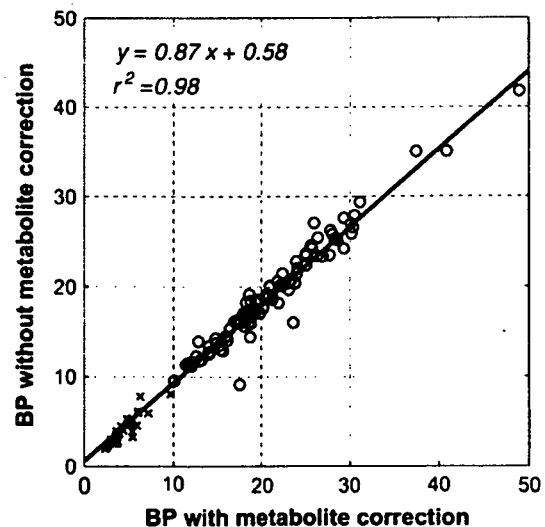
Fig. 5. Comparison of binding potentials, with and without metabolite correction, estimated by proposed full kinetic analysis. All ROIs obtained from each subject are plotted: circles represent data from the baseline condition, and crosses represent data from the haloperidol loading condition.
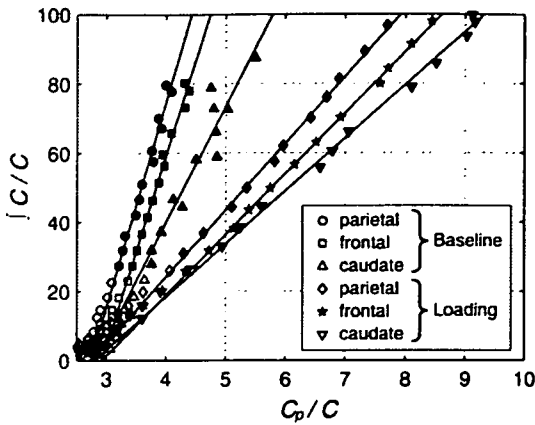
Fig. 6. Typical Logan plots. The plots for the parietal cortex, frontal cortex and caudate in baseline and haloperidol loading conditions are presented. $C$ and $C_p$ denote the measured time course of radioactivity in tissues and arterial plasma, respectively. Fitted lines derived from regression analysis using the data recorded from 30 to 90 min after administration of [11C] SA4503 are superimposed. Data used for the line estimation are shown as solid bullets.
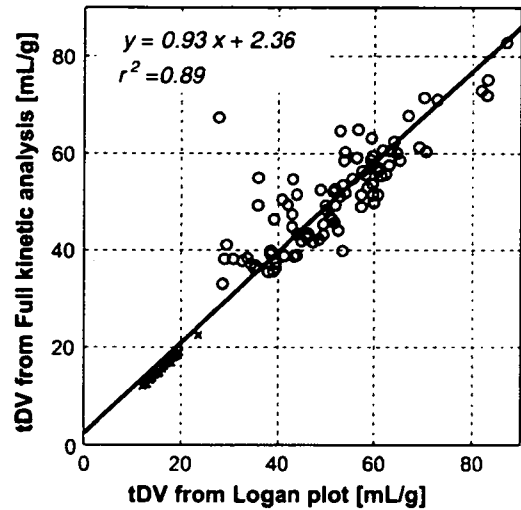


Fig. 8. Validation of the estimates of total distribution volumes. The total distribution volumes estimated by compartment model analysis (ordinate) were compared with those estimated by Logan plot analysis (abscissa). All ROIs obtained from all subjects are plotted: circles represent data from the baseline condition, and crosses represent data from the haloperidol loading condition.

between both estimates ($y=0.93x+2.36$, $r^2=0.89$). Compared with the tDVs estimated by NLE, those in the cerebellar vermis derived from Logan plot analysis were underestimated because of the noise included in the tTAC. Thus, the tDVs in the cerebellar vermis were not used in this validation of the NLE method.

Images of tDV are shown in Fig. 9. tDV values were large in the cortices and basal ganglia and small in the white matter, and they significantly decreased after haloperidol loading. tDV values in Fig. 9 were smaller than those in the NLE (Table 1).

## Discussion

The σ1R is related to some diseases of the central nervous system, and [11C]SA4503 is used as a probe for mapping σ1Rs in the human brain. Throughout this study, a way of kinetically analyzing of [11C]SA4503 has been considered.
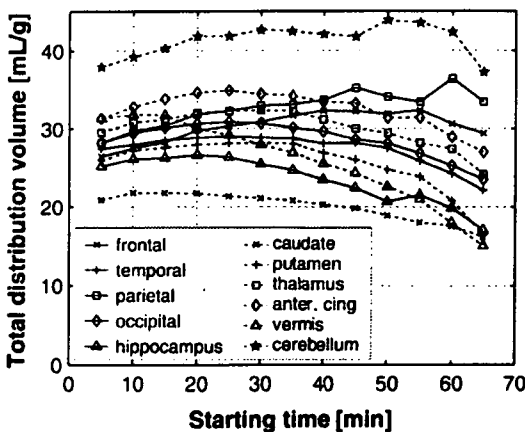


Fig. 7. Effects of starting time on the estimation of total distribution volume (tDV). A Logan plot was applied using varying starting times for the estimation. The starting time varied from 5 to 65 min, and the end time was fixed at 90 min.

First, compartmental analysis of [11C]SA4503 in the brain was investigated. Theoretically, six parameters should be estimated in the two-tissue three-compartment model: $K_1$, $k_2$, $k_3$, $k_4$, delay, and blood volume. However, under an exact measurement situation, it is not feasible to estimate all the parameters simultaneously. In general, an estimation algorithm suffers from instability and dependency on the initial guess because of the noise in the tTAC. Additionally, the sensitivity of $k$ parameters to a cost function for parameter estimation is much lower than that of blood volume or delay. Therefore, the practical implementation of the kinetic analysis means that parameters are estimated based on physiological aspects of the target neuroreceptor and the signal-to-noise ratio in the measured tTAC. Thus, reduction of the number of estimated parameters should be considered. It is physiologically reasonable to assume that blood volume is common to all brain regions, and this was fixed at 3% (Martin et al., 1987). The delay between tTAC and pTAC was also more sensitive than $k$ parameters, and a sensitive parameter was converged on more quickly than the other parameters. In this study, five parameters ($K_1$, $k_2$, $k_3$, $k_4$, and delay) were estimated simultaneously in the first step of the estimation, then the delay estimate was used in the fixed parameters of the second step. Only four $k$ parameters were estimated in the second step. Consequently, stable compartment model analysis could be accomplished and 94% of estimations could be considered reliable because they led to convergence within a 10% neighboring region of the estimation.

Second, the compartmental analysis was validated using the Logan plot. The Logan plot can estimate a stable tDV because it is implemented with a linear estimation, so it does not suffer from the problems of initial guess and misconvergency to a local minimum. As shown in Fig. 6, linear relationships were established in Logan plot analysis, demonstrating that the Logan plot is applicable to the analysis of [11C]SA4503. As pointed out by Ichise et al. (2002), the starting time for the Logan plot affects the estimates if a tTAC showed slow kinetics. As shown in Fig. 4, the time course and
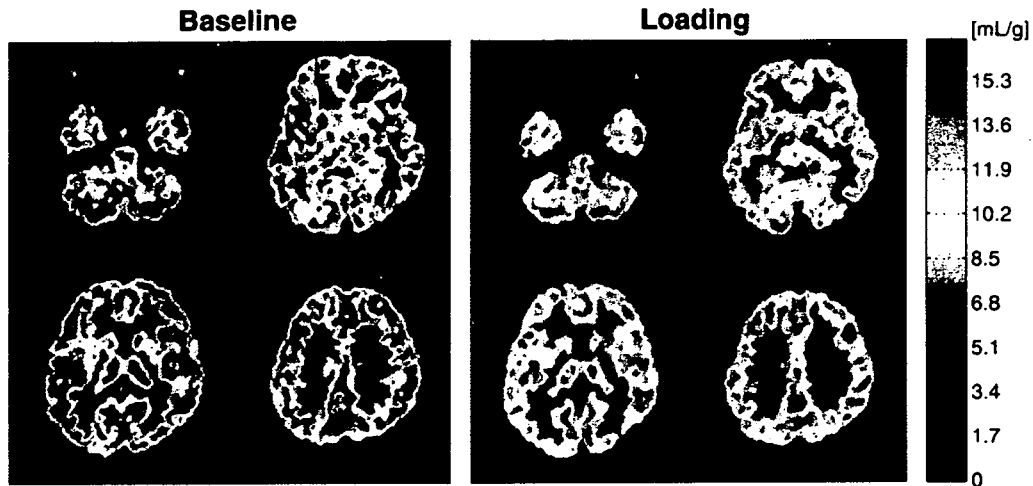
**Baseline**      **Loading**     [mL/g]



Fig. 9. Image of total distribution volumes derived with a Logan plot. The data from 30 to 90 min were applied to the Logan plot analysis.

activity of [¹¹C]SA4503 in the brain were slow and/or tended to increase after the first rapid incorporation; therefore, the starting time was sensitive to the estimated tDV. Acceptable candidates, within 20 to 40 min, were used as starting times for the Logan plot and were examined. No significant difference in estimated tDVs occurred by changing the starting time from 20 min to 40 min.

As shown in Fig. 8, the estimated tDVs from the kinetic analysis with NLE and Logan plot analysis matched each other well. The Logan plot offered stable estimates of tDV and gave more validity to our method for the kinetic analysis. The subsequent tDV images of the human brain (Fig. 9), as well as the regional distribution of the ROI-based BP (Table 1), may resemble the distribution patterns of the binding of radioligands in primate brains using an *in vitro* binding assay and autoradiography, where sigma receptors are widely distributed with different densities (Weissman et al., 1988; Shibuya et al., 1992; Mash and Zabetian, 1992). However, the radioligands used *in vitro* were not selective enough for σ1R when compared with [¹¹C]SA4503 in the present study. [¹¹C]SA4503-PET apparently exhibited the highest tDV in the cerebellum, but BP in the cerebellum was not highest (Table 1). A SPECT ligand [¹²³I] TPCNE also showed high binding in the cerebellum of humans (Stone et al., 2006); however, compared to these two radioligands, the uptake (not quantitative binding parameters) of a PET ligand [¹⁸F]FBFPA in the cerebellum was relatively low in monkeys (Mach et al., 2005). In our previous study of [¹¹C] SA4503-PET using monkeys, the highest BP of [¹¹C]SA4503 was observed in the hippocampus as shown in the human brain (Table 1) followed by the cingulated cortex, frontal cortex, thalamus and cerebellar hemisphere (Kawamura et al., 2003). Taken together these findings, there may be a slight species difference between humans and non-human primates.

A haloperidol loading study also confirms the validity of our proposed method. In this study, the available binding sites of σ1Rs in the brain were considerably lowered by partial blockade with an oral administration of haloperidol (3 mg, 18 h prior the PET scan) (Ishiwata et al., 2003); however, BP and tDV were evaluated with similar accuracy, as observed in the baseline (Figs. 5, 6 and 8). These results indicate that the reduced densities of σ1Rs in brains from individuals with neurological disorders can be reliably evaluated.

When we assessed the σ1R occupancy with haloperidol, when the occupancy rate was calculated to be 100×[(BP in baseline)−(BP in haloperidol loading)]/(BP in baseline), the σ1R occupancy rates were about 80% in all regions investigated: the highest occupancy was 87% in the parietal and the lowest was 77% in the thalamus. Therefore, the preliminary experiment with haloperidol loading also demonstrates that [¹¹C]SA4503-PET could be useful for evaluating the therapeutic effects of the drugs and for the development of new drugs in term of the measurement of σ1R occupancy rates. It should be noted that haloperidol is a nonselective antagonist for sigma receptors and also binds other receptors such as dopamine D₂-like receptors. Therefore, the present study does not demonstrate the σ1R-selective binding of [¹¹C]SA4503. However, the use of haloperidol as a blocker is interesting because it is clinically used (usually 3–10 mg) as a typical antipsychotic drug. We previously reported that the σ1R blockade by haloperidol in the mouse brain continued slightly longer than the dopamine D₂-like receptor blockade (Ishiwata et al., 2003). Recently, we confirmed that the receptor occupancy rate for σ1R (approximately 80%) in the human brain was higher than that for dopamine D₂-like receptor (approximately 60%) after the oral administration of haloperidol (3 mg) in a similar experimental protocol (Ishiwata et al., 2006). Concerning the haloperidol challenge, Stone et al. (2006) also demonstrated that an oral administration of haloperidol (2.5 mg, approximately 1 h before the SPECT scan) greatly decreased the binding of [¹²³I]TPCNE to σ1Rs with a different extent in the brain regions: from 42% reduction in the cerebellum to 73% reduction in the thalamus (*n*=1). The blockade for σ1Rs by [¹²³I]TPCNE seems slightly smaller than that by [¹¹C]SA4503. A main reason for the difference may be the period between haloperidol administration and imaging, i.e., a 1-h interval may be early for an oral administration. The other reason may be due to selectivity of the two radioligands. The sigma₁/sigma₂ selectivity for [¹¹C]SA4503 was 106 (Matsuno et al., 1996), while that for [¹²³I]TPCNE was 58 (Waterhouse et al., 1997). The affinity of [¹¹C]SA4503 for sigma₂ receptor (IC₅₀=1784 nM) was much lower than that of [¹²³I]TPCNE (Ki=38.8 nM) (Waterhouse et al., 1997).

In Logan plot analysis, the noise of tTAC causes an underestimation of tDV (Slifstein and Laruelle, 2000). In ROI-based analysis, the mean of the dynamic image was used because it

reduced the noises. However, because the noise remained high in the tTACs for small regions of the brain, it caused an underestimation of tDV in the cerebellar vermis, which was the smallest region. Additionally, the tDV of the parametric images, which were affected by the noise of the tTACs, were estimated to be smaller than the estimates for the ROIs. Nevertheless, Logan plot analysis easily provides images of tDV. As shown in Table 1, the distribution volume of the ligand in the free component was much smaller than the tDV, which demonstrates that the specific binding of [$^{11}$C]SA4503 reached about 95% of tDVs in all brain regions investigated. Therefore, tDV images essentially reflect the density of σ1Rs. Thus, Fig. 9 indicates that σ1Rs are widely spread with different densities in the whole brain and that a significant decrement of tDVs occurred by blockade with haloperidol.

Let us consider the requirement of metabolite correction for pTAC. Metabolite correction is usually required for kinetic analysis to compensate for the radioligand that is metabolized peripherally. As shown in Fig. 3, the intact form of [$^{11}$C]SA4503 makes up about 90% of the radioactivity in arterial plasma over 60 min, suggesting that a slow peripheral metabolism of [$^{11}$C]SA4503 occurs. Moreover, from a practical point of view, precise measurement of small amounts of labeled metabolites is difficult, especially over time, because of the very rapid clearance of [$^{11}$C] SA4503 from plasma. Therefore, the omission of metabolite correction is appropriate. The BP values without metabolite correction were 13% lower than those with metabolite correction; however, BP values with and without metabolite correction showed an almost identical relationship in all subjects, all ROIs and the two conditions: baseline and haloperidol loading. Therefore, metabolite correction can be reasonably avoided. It should be noted that [$^{11}$C]SA4503 was metabolically more stable in humans than in rats (the intact form in plasma, approximately 95% versus 80%, respectively, of 30 min postinjection), and the haloperidol challenge did not alter the metabolism. Stability of [$^{11}$C]SA4503 in plasma may be explained by the fact that the tracer mainly underwent biliary excretion (Kawamura et al., 2000b; van Waarde et al., 2004), which might result in scarce recirculation of labeled metabolites into the plasma.

## Conclusion

We conclude that our proposed method using a two-tissue three-compartment model is appropriate to provide BP and tDV for the kinetic analysis of [$^{11}$C]SA4503-PET in human brain tissue. The tDV derived matched well with that derived from the Logan plot analysis, whose images enable visualization of the spatial distribution of σ1Rs. The reduced binding sites of σ1Rs by haloperidol challenge were appropriately evaluated. Moreover, comparison of BPs calculated with and without metabolite correction for the plasma input function indicated that the metabolite correction could be omitted. We concluded that this method enables the quantitative analysis of σ1Rs in the human brain.

## Acknowledgments

## References

Ardekani, B.A., Braun, M., Hutton, B.F., Kanno, I., Iida, H., 1995. A fully automatic multimodality image registration algorithm. J. Comput. Assist. Tomogr. 19, 615–623.

Bard, Y., 1974. Weighted least squares. Nonlinear Parameter Estimation. Academic Press, New York, pp. 56–57. Chap. 4-3.

Coleman, T., Branch, M.A., 1999. Optimization Toolbox User's Guide. MathWorks Inc., Natick, MA.

Fujiwara, T., Watanuki, S., Yamamoto, S., Miyake, M., Seo, S., Itoh, M., Ishii, K., Orihara, H., Fukuda, H., Satoh, T., Kitamura, K., Tanaka, K., Takahashi, S., 1997. Performance evaluation of a large axial field-of-view PET scanner: SET-2400W. Ann. Nucl. Med. 11, 307–313.

Hashimoto, K., Ishiwata, K., 2006. Sigma receptor ligands: possible application as therapeutic drugs and as radiopharmaceuticals. Curr. Pharm. Des. 12, 3915–3928.

Helmeste, D.M., Tang, S.W., Bunney Jr., W.E., Potkin, S.G., Jones, E.G., 1996. Decrease in sigma but no increase in striatal dopamine D4 sites in schizophrenic brains. Eur. J. Pharmacol. 314 (3), R3–R5.

Ichise, M., Toyama, H., Innis, R.B., Carson, R.E., 2002. Strategies to improve neuroreceptor parameter estimation by linear regression analysis. J. Cereb. Blood Flow Metab. 22, 1271–1281.

Ishiwata, K., Tsukada, H., Kawamura, K., Kimura, Y., Nishiyama, S., Kobayashi, T., Matsuno, K., Senda, M., 2001. Mapping of CNS sigma$_1$ receptors in the conscious monkey: preliminary PET study with [$^{11}$C] SA4503. Synapse 40, 235–237.

Ishiwata, K., Kawamura, K., Kobayashi, T., Matsuno, K., 2003. Sigma$_1$ and dopamine D$_2$ receptors occupancy in the mouse brain after a single administration of haloperidol and two dopamine D$_2$-like receptor ligands. Nucl. Med. Biol. 30, 429–434.

Ishiwata, K., Oda, K., Sakata, M., Kimura, Y., Kawamura, K., Oda, K., Sasaki, T., Naganawa, M., Chihara, K., Okubo, Y., Ishii, K., 2006. A feasibility study of [$^{11}$C]SA4503-PET for evaluating sigma$_1$ receptor occupancy by neuroleptics: the binding of haloperidol to sigma$_1$ and dopamine D$_2$-like receptors. Ann. Nucl. Med. 20, 569–573.

Jansen, K.L., Faull, R.L., Storey, P., Leslie, R.A., 1993. Loss of sigma binding sites in the CA1 area of the anterior hippocampus in Alzheimer's disease correlates with CA1 pyramidal cell loss. Brain Res. 623, 299–302.

Junien, J.L., Leonard, B.E., 1989. Drugs acting on sigma and phencyclidine receptors: a review of their nature, function and possible therapeutic importance. Clin. Neuropharmacol. 12, 353–374.

Kawamura, K., Ishiwata, K., Shimada, Y., Kimura, Y., Kobayashi, T., Matsuno, K., Homma, Y., Senda, M., 2000a. Preclinical evaluation of [$^{11}$C]SA4503: radiation dosimetry, in vivo selectivity and PET imaging of sigma$_1$ receptors in the cat brain. Ann. Nucl. Med. 14, 285–292.

Kawamura, K., Ishiwata, K., Tajima, H., Ishii, S., Matsuno, K., Homma, Y., Senda, M., 2000b. In vivo evaluation of [$^{11}$C]SA4503 as a PET ligand for mapping CNS sigma$_1$ receptors. Nucl. Med. Biol. 27, 255–261.

Kawamura, K., Kimura, Y., Tsukada, H., Kobayashi, T., Nishiyama, S., Kakiuchi, T., Ohba, H., Harada, N., Matsuno, K., Ishii, K., Ishiwata, K., 2003. An increase of sigma$_1$ receptors in the aged monkey brain. Neurobiol. Aging 24, 745–752.

Kimura, Y., Ishii, K., Fukumitsu, N., Oda, K., Sasaki, T., Kawamura, K., Ishiwata, K., 2004. Quantitative analysis of adenosine A$_1$ receptors in human brain using positron emission tomography and [1-methyl-$^{11}$C]8-dicyclopropylmethyl-1-methyl-3-propylxanthine. Nucl. Med. Biol. 31, 975–981.

Koeppe, R.A., Holthoff, V.A., Frey, K.A., Kilbourn, M.R., Kuhl, D.E., 1991. Compartmental analysis of [$^{11}$C]flumazenil kinetics for the estimation of ligand transport rate and receptor distribution using positron emission tomography. J. Cereb. Blood Flow Metab. 11, 735–744.

Logan, J., Fower, J.S., Volkow, N.D., Wolf, A.P., Dewey, S.L., Schlyer, D.J., MacGregor, R.R., Hitzemann, R., Bendriem, B., Gatley, S.J., Christman, D.R., 1990. Graphical analysis of reversible radioligand binding from time–activity measurements applied to [N-^{11}C-methyl]-(−)-cocaine PET studies in human subjects. J. Cereb. Blood Flow Metab. 10, 740–747.

Mach, R.H., Gage, H.D., Buchheimer, N., Huang, Y., Kuhner, R., Wu, L., Morton, T.E., Ehrenkaufer, R.L., 2005. N-[^{18}F]4′-fluorobenzylpiper-idin-4yl-(2-fluorophenyl) acetamide ([^{18}F]FBFPA): a potential fluorine-18 labeled PET radiotracer for imaging sigma-1 receptors in the CNS. Synapse 58, 267–274.

Martin, W.R.W., Powers, W.J., Raichle, M.E., 1987. Cerebral blood volume measured with Inhaled $C^{15}O$ and positron emission tomography. J. Cereb. Blood Flow Metab. 7, 421–426.

Mash, D.C., Zabetian, C.P., 1992. Sigma receptors are associated with cortical limbic areas in the primate brain. Synapse 12, 195–205.

Matsuno, K., Mita, S., 1998. SA4503: a novel sigma_1 receptor agonist. CNS Drug Rev. 4, 1–24.

Matsuno, K., Nakazawa, M., Okamoto, K., Kawashima, Y., Mita, S., 1996. Binding properties of SA4503, a novel and selective σ_1 receptor agonist. Eur. J. Pharmacol. 306, 271–279.

Mintun, M.A., Raichle, M.E., Kilbourn, M.R., Wooten, G.F., Welch, M.J., 1984. A quantitative model for the in vivo assessment of drug binding sites with positron emission tomography. Ann. Neurol. 15, 217–227.

Mishina, M., Ishiwata, K., Ishii, K., Kitamura, S., Kimura, Y., Kawamura, K., Oda, K., Sasaki, T., Sakayori, O., Hamamoto, M., Kobayashi, S., Katayama, Y., 2005. Function of sigma_1 receptors in Parkinson's disease. Acta Neurol. Scand. 112, 103–107.

Nelder, J., Mead, R., 1965. A simplex method for function minimization. Comput. J. 7, 308–313.

Shibuya, H., Mori, H., Toru, M., 1992. Sigma receptors in schizophrenic cerebral cortices. Neurochem. Res. 17, 983–990.

Slifstein, M., Laruelle, M., 2000. Effects of statistical noise on graphic analysis of PET neuroreceptor studies. J. Nucl. Med. 41, 2083–2088.

Stone, J.M., Arstad, E., Erlandsson, K., Waterhouse, R.N., Ell, P.J., Pilowsky, L.S., 2006. [^{123}I]TPCNE-a novel SPET tracer for the sigma-1 receptor: first human studies and in vivo haloperidol challenge. Synapse 60, 109–117.

Su, T.P., 1993. Delineating biochemical and functional properties of sigma receptors: emerging concepts. Crit. Rev. Neurobiol. 7, 187–203.

Su, T.P., Hayashi, T., 2003. Understanding the molecular mechanism of sigma-1 receptors: towards a hypothesis that sigma-1 receptors are intracellular amplifiers for signal transduction. Curr. Med. Chem. 10, 2073–2080.

van Waarde, A., Buursma, A.R., Hospers, G.A.P., Kawamura, K., Kobayashi, T., Ishii, K., Oda, K., Ishiwata, K., Vaalburg, W., Elsinga, P.H., 2004. Tumor imaging with 2 σ-receptor ligands, [^{18}F]FE-SA5845 and [^{11}C]SA4503: a feasibility study. J. Nucl. Med. 45, 1939–1946.

Watabe, H., Channing, M.A., Der, M.G., Adams, H.R., Jagoda, E., Herscovitch, P., Eckelman, W.C., Carson, R.E., 2000. Kinetic analysis of the 5-HT$_{2A}$ ligand [^{11}C]MDL 100,907. J. Cereb. Blood Flow Metab. 20, 899–909.

Waterhouse, R.N., Mardon, K., Giles, K.M., Collier, T.L., O'Brien, J.C., 1997. Halogenated 4-(phenoxymethyl)piperidines as potential radiola-beled probes for sigma-1 receptors: in vivo evaluation of [^{123}I]-1-(iodopropen-2-yl)-4-[(4-cyanophenoxy)methyl]piperidine. J. Med. Chem. 40, 1657–1667.

Weissman, A.D., Su, T.P., Hedreen, J.C., London, E.D., 1988. Sigma receptors in post-mortem human brains. J. Pharmacol. Exp. Ther. 247, 29–33.

Weissman, A.D., Casanova, M.F., Kleinman, J.E., London, E.D., De Souza, E.B., 1991. Selective loss of cerebral cortical sigma, but not PCP binding sites in schizophrenia. Biol. Psychiatry 29, 41–54.
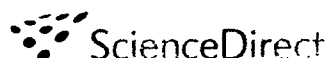
## Research Report

# A comparative study of bioradiography in human brain slices and preoperative PET imaging

Toru Sasaki[a,b,*], Tadashi Nariai[c], Taketoshi Maehara[c], Katsushige Sato[d], Keiich Oda[b], Kenji Ishii[b]

[a]Research Team for Molecular Biomarker, Tokyo Metropolitan Institute of Gerontology, Itabashi-ku, Tokyo 173-0015, Japan
[b]Positron Medical Center, Tokyo Metropolitan Institute of Gerontology, Itabashi-ku, Tokyo 173-0015, Japan
[c]Department of Neurosurgery, Tokyo Medical and Dental University, Bunkyo-ku, Tokyo 113-8519, Japan
[d]Department of Physiology, Tokyo Medical and Dental University, Bunkyo-ku, Tokyo 113-8519, Japan

ARTICLE INFO

ABSTRACT

Novel autoradiography (bioradiography) images in human neocortical brain slices which were obtained at operation from seven patients with intractable epilepsy who had received a 2-[$^{18}$F]fluoro-2-deoxy-D-glucose-positron emission tomography (FDG-PET) examination preoperatively, were acquired in Krebs–Ringer medium (control condition) and that with high K$^+$ (high K$^+$ condition) containing FDG and compared with FDG-PET uptake. The FDG uptake images in rat brain slices were also acquired as a reference and compared with that in humans. In the slices incubated under high K$^+$, FDG uptake in both human and rat gray matter was significantly enhanced, whereas that in the white matter was not. But the variance of uptake was larger in humans than the rats. This might indicate the different degree of progress of epilepsy in the sampled brain tissues. The uptake rates of FDG in human gray matter under the control condition showed an inverse correlation with those seen in PET, which were evaluated as sampled and contralateral gyri (SG/CG) and sampled gyri and cerebellar cortex (SG/CB) ratio. On the contrary, it showed a weak positive correlation with PET under the high K$^+$ condition. The uptake rates of FDG in human gray matter expressed as a high K$^+$/control ratio, closely matched that observed by FDG-PET, which were evaluated as the SG/CG ratio and the SG/CB ratio. Our experimental system provides useful information for the interpretation of PET data in epileptics and the theoretical basis to interpret the results of metabolic studies using living human brain tissues for further use in pharmacological manipulation.

© 2007 Elsevier B.V. All rights reserved.

## Introduction

Bioradiography is a novel autoradiographic method to estimate metabolism and physiological function in living tissues using positron emitter-labeled compounds for positron emission tomography (PET) (Matsumura et al., 1995; Murata et al., 1996; Sasaki et al., 2002a,b). It offers the following advantages: (1) dynamic changes in metabolic activity can be followed in living tissue, (2) environmental conditions of tissue slices can be easily controlled as required, and (3) radioligand delivery to

* Corresponding author. Present address: Research Team for Molecular Biomarker, Tokyo Metropolitan Institute of Gerontology, Itabashi-ku, Tokyo 173-0015, Japan.
E-mail address: tsasaki@center.tmig.or.jp (T. Sasaki).

the tissue is not influenced by blood flow. This method has been used to study glucose metabolism, neuroreceptor assays and neurotransmitter release in animal brain tissues (Matsumura et al., 1995; Murata et al., 1996; Sasaki et al., 2002a,b).

Surgery has been recognized as an effective treatment for certain epileptic patients, such as those with medically intractable temporal lobe epilepsy (TLE) (Cascino et al., 2004). Presurgical imaging using PET, single photon emission tomography, and magnetic resonance imaging (MRI) is used to assess the feasibility of surgery and to decide the scale of excision in regions with spike activity (Casse et al., 2002; Matheja et al., 2000). The brain regions estimated to have low glucose metabolism by 2-[$^{18}$F]fluoro-2-deoxy-D-glucose (FDG)-PET are diagnosed as the excision extent including epileptogenic foci (Casse et al., 2002). Noninvasive molecular-imaging techniques such as PET have potential roles in disease diagnosis and therapy, but diagnosis as in the case of epilepsy is influenced by several factors and problems, for example, biodegradation of the radioligand, influence of blood flow on radioligand delivery, and limited spatial resolution. In order to confirm PET diagnosis, glucose metabolism in living human brain tissue in vitro was compared with preoperative FDG-PET findings using bioradiography with FDG in brain slices obtained at operation from patients with intractable epilepsy.

## Results

The experimental flowchart is shown in Fig. 1. All seven patients underwent excisions of pathological lesions and the area with epileptogenecity surrounding them identified by presurgical FDG-PET, MRI, and intraoperative cortical electro-encephalography (EcoG). In all cases, a significant amelioration of seizures was achieved by surgery. This indicated that the epileptic foci and the pathological brain surrounding them were precisely detected and resected. In all the patients, cortical gyri sampled for slice analysis were not the epileptic foci themselves but the gyri surrounding the focus from where an abnormal EcoG pattern was recorded. Though three of seven patients harbored low-grade gliomas, the proliferation rate of tumor cells determined from the labeling rate with a monoclonal antibody (MIB-1) against nuclear antigen Ki-67 (Ki labeling index) was very low (<1% in two and 5% in one) and therefore none of them were invasive tumors. No tumor cells were identified in the sampled gyri of three of tumor patients. Therefore, we concluded that the sampled cortical gyri used for autoradiographical analysis was the cortex outside the main lesions but influenced by chronic epileptic conditions (Table 1).

As shown in Table 2 and Fig. 5, FDG uptake in the sampled gyri was lower than that in the contralateral gyri or cere-
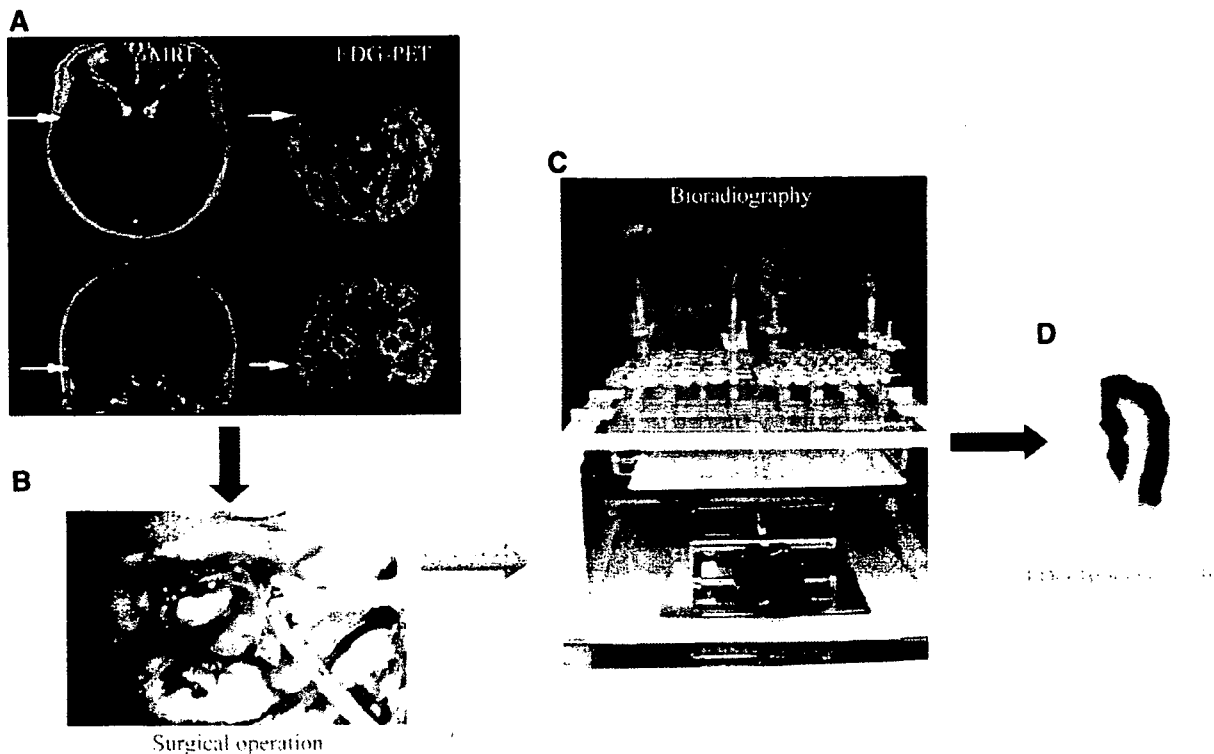


Fig. 1 – Flowchart for bioradiography in human brain slices. (A) The presurgical evaluation of patients with medically intractable epilepsy was performed with FDG-PET co-registered to MRI. FDG-PET showed hypo-glucose metabolism in the right temporal cortex (arrow). (B) Epileptic foci and the epileptogenic cortical gyrus surrounding them were surgically excised (arrow). The former was subjected to routine pathological analysis and the latter to bioradiographical analysis. (C) Bioradiography for analysis in vitro using human and animal brain slices. (D) FDG bioradiographic image of an excised human brain slice.

| Case number | Age (years) and sex | Age at seizure onset (years) | Side of lesions | Pathology (Ki labeling index) | Surgical outcome (follow-up periods) |
|---|---|---|---|---|---|
| | | | | **Table 1 – Patient characteristics** | |
| 1 | 35, Female | 26 | Right | Dysembryoplastic neuroepithelial tumor (<1%) | Free (4 years) |
| 2 | 25, Male | 20 | Left | Cavernous angioma | Free (4 years) |
| 3 | 48, Male | 20 | Left | Pleomorphic xanthoastrocytoma (5%) | Free (4 years) |
| 4 | 27, Female | 13 | Left | Hippocampal sclerosis | Free (4 years) |
| 5 | 26, Female | 12 | Left | Hippocampal sclerosis | Free (3 years) |
| 6 | 25, Female | 15 | Left | Hippocampal sclerosis | Free (3 years) |
| 7 | 19, Female | 17 | Left | Low grade astrocytoma (<1%) | 1–2/year (4 years) |

bellum. This result also indicated that all the sampled gyri were pathological cerebral cortex to different degrees among patients. Typical uptake patterns of FDG in human and rat brain slices are shown in Figs. 2 and 3. The uptake in human and rat brain under control and high $K^+$ conditions increased continuously up to 250 min. The white matter showed slightly greater uptake than the gray matter under the control condition (Figs. 2 and 3). The uptake of FDG in human gray matter was significantly enhanced by a neuro-stimulant, high $K^+$ ($P=0.0049$ from control gray matter with an outlier and $P=0.0050$ without an outlier), whereas that in the white matter was not enhanced (Fig. 4). The uptake in rat gray matter was also enhanced by high $K^+$ ($P=0.0051$ from control gray matter). The average rate of uptake per pixel per minute in high $K^+$-treated human (including outlier) and rat brain was increased 7.0- and 7.6-fold compared to the control level, respectively (Fig. 4). The uptake in human gray matter under both control and high $K^+$ conditions did not differ significantly from that in rat (Fig. 4). However, significant differences between rat and human tissues were found in variance under the control condition ($P=0.0001$) and the control/high $K^+$ ratio ($P=0.0005$).

The relationship between FDG uptake in PET and bioradiography is shown in Fig. 5. The outlier was contained in the human data (arrow in Fig. 5). The relationship was analyzed between FDG-PET and FDG bioradiographic data with an outlier (7 patients) and without (6 patients). The rates of uptake in gray matter of brain slices under the control condition showed an inverse correlation with those seen in PET, evaluated as the sampled and contralateral gyri (SG/CG)

ratio ($r=0.936$, $P=0.0007$ with an outlier and $r=0.814$, $P=0.0494$ without) and the sampled gyri and cerebellar cortex (SG/CB) ratio ($r=0.788$, $P=0.0330$ with an outlier and $r=0.896$, $P=0.0156$ without) (Fig. 5). In contrast, it showed a weak positive correlation with PET under the high $K^+$ condition, but this was not statistically significant. The rates of uptake in gray matter of brain slices, expressed as the high $K^+$/control ratio, correlated with those seen in PET, evaluated as the SG/CG ratio ($r=0.844$, $P=0.0134$ with an outlier and $r=0.691$, not significant without) and the SG/CB ratio ($r=0.904$, $P=0.0028$ with an outlier and $r=0.828$, $P=0.0417$ without) (Fig. 5).

## Discussion

We have examined the bioradiographic images of FDG in human and rat brain slices under the control and high $K^+$ conditions and compared them with FDG-PET. Normal human brain cannot be used for in vitro studies as a reference for ethical reasons. We speculated that brain tissue from animals with well-controlled breeding could be a substitute for human brain tissues, and the uptake of FDG in animal tissues would show little variance because there is no morbidity. On the other hand, the variance in epileptic brain tissue shows a large degree of variance, depending on the progress of the epilepsy. Indeed, significant differences in variance between rat and human tissues were found in the uptake of FDG under the control condition and in which expressed the high $K^+$/control ratio.

| Case number | PET[a] | | Bioradiography[b] | | | Time interval between PET and bioradiography |
|---|---|---|---|---|---|---|
| | SG/CG ratio | SG/CB ratio | Control | High $K^+$ | High $K^+$/control ratio | |
| | | | | **Table 2 – Details of the PET and bioradiography data for seven patients** | | |
| 1 | 0.9593 | 0.8741 | 1.43 | 14.23 | 9.95 | <1 month |
| 2 | 0.8273 | 0.7895 | 2.92 | 10.75 | 3.68 | 1 month |
| 3 | 0.7409 | 0.7853 | 3.16 | 15.75 | 4.98 | <1 month |
| 4 | 0.8746 | 0.9029 | 1.19 | 14.23 | 11.96 | 7 years |
| 5 | 0.8868 | 0.8545 | 2.34 | 16.47 | 7.04 | 3 months |
| 6 | 0.9193 | 0.9918 | 1.16 | 12.10 | 10.43 | 2 months |
| 7 | 0.5479 | 0.7063 | 11.55 | 6.35 | 0.55 | <1 month |

[a] FDG uptake in PET was calculated as the ratio between the sampled and contralateral gyrus (SG/CG) or the sampled gyrus and cerebellum (Sg/CB).
[b] FDG bioradiographic uptake in gray matter of the brain slices was expressed as the rate of uptake per pixel per minute (counts/pixel/min) in control medium, that in high $K^+$ medium and the uptake ratio between high $K^+$/control media.
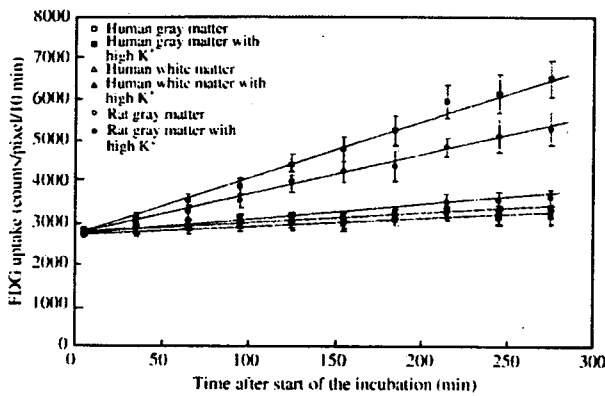
**Fig. 2 – Time-courses of FDG uptake in human and rat brain slices (control and high K⁺ treatment).**

FDG uptake in the gray matter was significantly enhanced (seven times the control) by high K⁺, whereas that in the white matter was not enhanced compared to the control condition. In the control condition, FDG uptake was slightly lower in gray matter than white matter (Figs. 2–4). A higher metabolic rate of FDG in gray matter than white matter was observed in PET studies, but the ratio of gray/white matter FDG metabolic rates was only about 2 (Huang et al., 1980; Reivich et al., 1985). The limited spatial resolution of PET introduces a partial volume effect, thereby causing an admixture of FDG metabolic rates in gray and white matter regions, and this might account for the discrepancy. Another factor could be the K⁺ concentration. The resting extracellular K⁺ concentration in the brain *in vivo*
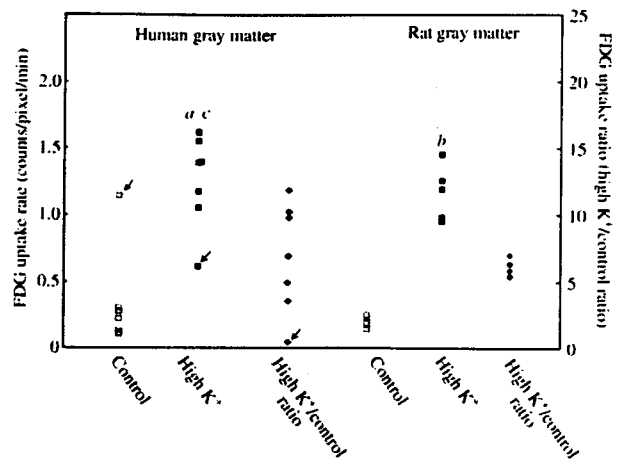


**Fig. 4 – Rate of FDG uptake in control and high K⁺-treated human and rat brain slices. The bioradiographic uptake in tissue slices was expressed as the rate of uptake per pixel per minute (counts/pixel/min) in control medium (left), that in high K⁺ medium (middle), and the uptake ratio between high K⁺/control media (right). The values are the mean±SD for 7 patients and 6 rats. Statistical significance was determined by the Wilcoxon/Kruskal–Wallis test for differences of data with an outlier (arrow) ($^aP$=0.0049 from control human gray matter and $^bP$=0.0051 from control rat gray matter) and without an outlier ($^cP$=0.0050 from control human gray matter). Significant differences in variance between rat and human tissues were found in FDG uptake under the control condition ($P$=0.0001) and the control/high K⁺ ratio ($P$=0.0005).**
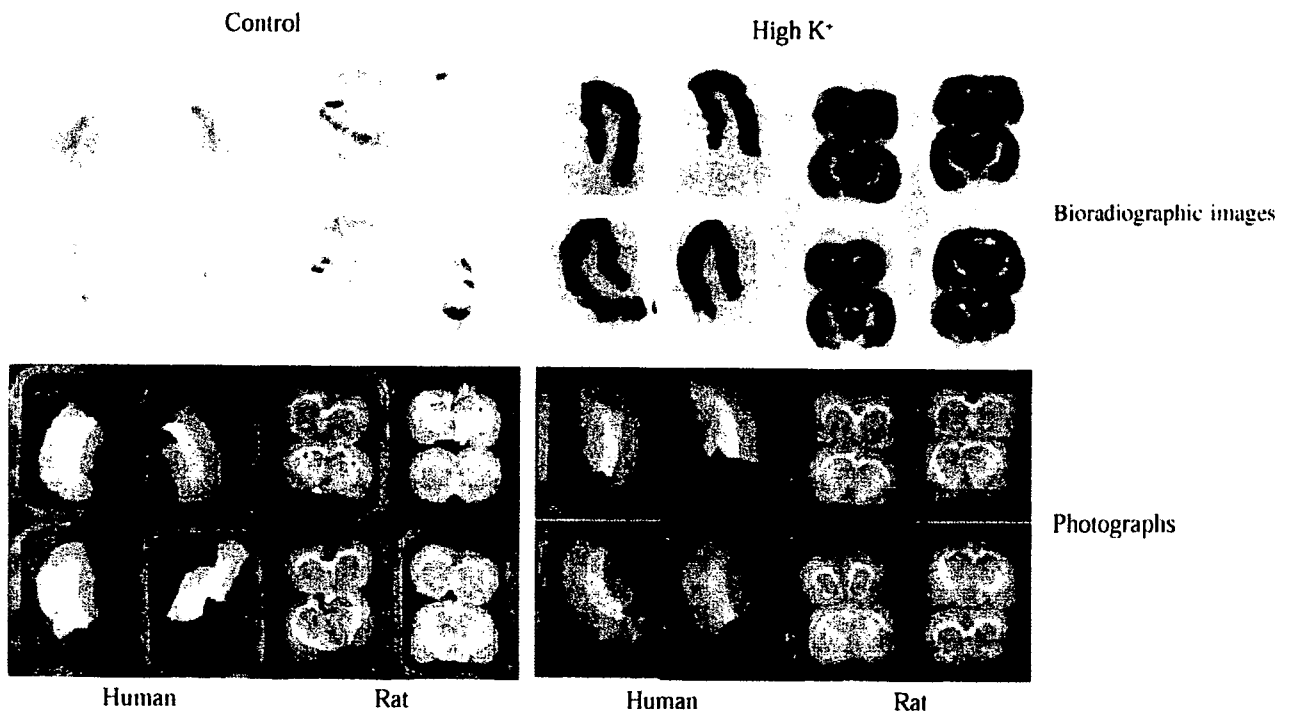


**Fig. 3 – Bioradiographic images at the 9th exposure (240–250 min) and photographs of control and high K⁺-treated human and rat brain slices.**

FDG-PET uptake ratio between sampled and contralateral gyrus values

FDG-PET uptake ratio between sampled gyrus cortex and cerebellum values
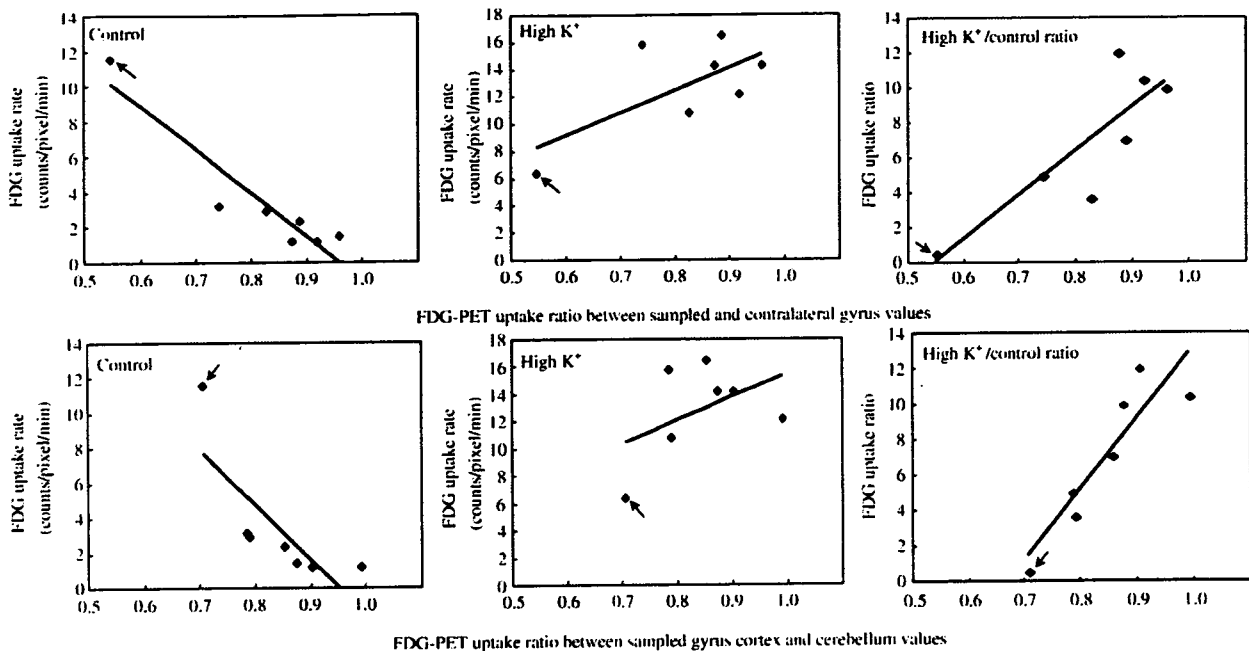
**Fig. 5** – Relationship between FDG uptake in PET and bioradiography. FDG uptake in PET was calculated as the ratio between that in the sampled and contralateral gyrus (SG/CG) (upper) or the sampled gyrus and cerebellar cortex (SG/CB) (lower). FDG bioradiographic uptake in gray matter of the brain slices was expressed as the rate of uptake per pixel per minute (counts/pixel/min) in control medium (left), that in high K$^+$ medium (middle), and the uptake ratio between high K$^+$/control media (right). The values compared favorably with SG/CG and SG/CB uptake ratios obtained by PET. The uptake rates of FDG in brain slices under the control condition showed an inverse correlation with those seen in PET, evaluated as the SG/CG ratio ($r=0.936$, $P=0.0007$ with an outlier and $r=0.814$, $P=0.0494$ without) and the SG/CB ratio ($r=0.788$, $P=0.0330$ with an outlier and $r=0.896$, $P=0.0156$ without). The uptake rates of FDG, expressed as the high K$^+$/control ratio, correlated with those seen in PET, evaluated as the SG/CG ratio ($r=0.844$, $P=0.0134$ with an outlier and $r=0.691$, not significant without) and the SG/CB ratio ($r=0.904$, $P=0.0028$ with an outlier and $r=0.828$, $P=0.0417$ without). An arrow indicates the outlier.

is normally ~3 mM and increases to 12 mM during neuronal activation. It rises as high as 50–80 mM in seizures (Somjen, 1975). In our study, the FDG-PET images were acquired in the interictal, not ictal, period. The K$^+$ concentration (50 mM) in the present in vitro study might correspond to the ictal concentration in vivo. This concentration might be higher than that in the interictal period. In the central nervous system, gray matter is constituted from perikaryons, unmyelinated fibers, protoplasmic astrocytes, and microglia, and white matter from myelinated fibers, oligodendrocytes, fibrous astrocytes and microglia (Graham and Lantos, 2002). The greater metabolic rate of glucose and higher sensitivity to high K$^+$ in gray matter is explained by the high density of neurons, as well as the sensitivity of neurons to high K$^+$ and the insensitivity of neuroglia (Takahashi et al., 1995; Sokoloff et al., 1996; Sokoloff, 1999; Honegger and Pardo, 1999).

Low glucose metabolism in epileptic brain regions including foci has been detected by FDG-PET (Huang et al., 1980; Casse et al., 2002). In all seven patients who underwent excisions of epileptogenic foci and surrounding them identified by presurgical FDG-PET, the uptake of FDG was lower in the sampled gyrus than in the contralateral gyrus and cerebellum (Table 2 and Fig. 5). These uptake ratios for FDG-PET, correlated well with the uptake rates in gray matter of the

human brain slices expressed as a high K$^+$/control ratio (Fig. 5, right), and weakly correlated with those in brain slices under the high K$^+$ condition but not significantly (Fig. 5, middle). However, the uptake rates of FDG in gray matter of the human brain slices under the control condition showed an inverse correlation with those seen in PET (Fig. 5, left). These results indicated that normality in response ability to a neuro-stimulant such as high K$^+$ relates to FDG uptake in epileptic brain regions including foci and surrounding them by PET. The working brain in vivo responds to stimulants from outside of the brain via nerve fibers, but the number of input signals is restricted partially in brain slices in vitro. Glucose metabolism in brain slices under the control culture condition might be too silent compared to that in the working brain. Therefore, this condition could not reflect FDG uptake in vivo. Even in the control condition, the brain slices which had shown low FDG uptake in vivo, had high uptake rates (Fig. 5, left). Such high glucose metabolism might indicate an abnormal response to stimuli in epileptic brain regions. Brain slices from one of the seven patients (arrow in Figs. 4 and 5) showed rather abnormal glucose metabolism. In this case, the specimen had been taken from epileptic tissue surrounding a low-grade astrocytoma, and pathological examination demonstrated gliosis without either normal cortical structures or tumor cells. Brain slices of this patient showed high glucose metabolism even

in the control medium, but poor sensitivity to high $K^+$. This phenomenon can be explained in terms of the properties of glial cells.

In the brain of an epileptic patient, neuronal death and gliosis progress as a result of repeated excessive excitement of neurons (Cohen-Gadol et al., 2006; Velisek and Moshe, 2003). In Alzheimer's brain, the area of hypo-glucose metabolism in PET correlated with that of neuronal loss and the proliferation of glia (McGeer et al., 1986; Minoshima et al., 1999). In a presurgical evaluation of temporal lobe epilepsy, both FDG and [$^{11}$C] flumazenil PET reliably indicated the epileptogenic temporal lobe. Decreased [$^{11}$C]flumazenil binding simply reflects a loss of neurons expressing the benzodiazepine-GABA receptor, but the area of hypometabolism in FDG-PET was more extensive than the areas of the epileptogenic temporal lobe and the decreased [$^{11}$C]flumazenil binding (Debets et al., 1997). The neuroglia is known to be insensitive to extracellular $K^+$ (Takahashi et al., 1995; Sokoloff et al., 1996; Sokoloff, 1999; Honegger and Pardo, 1999). These results indicate that neuronal loss and gliosis in epileptogenic brain regions could be one reason for the hypo-glucose metabolism in PET.

As another explanation, impaired glutamatergic signaling is considered a mechanism of the hypo-glucose metabolism seen in FDG-PET. Glutamate is the principal excitatory transmitter within the vertebrate nervous system (Meldrum, 2000). During seizures, the glutamate concentration in epileptogenic brain regions increases to neurotoxic levels (During and Spencer, 1993). The increase in glutamate or its degradation product glutamine continues even after the seizures (Fazekas et al., 1995). Increased glutamate in epileptogenic brain regions is hypothesized to be due to slow rates of glutamate–glutamine cycling (Petroff et al., 2002). However, another report showed that glucose metabolism and glutamate cycling in epileptogenic brain using FDG-PET and 1H magnetic resonance spectroscopy (Pfund et al., 2000). The decrease in glucose metabolism and glutamate (NMDA) receptor demonstrated using FDG-PET, and [$^{11}$C]ketamine also indicates that glutamatergic signal transduction activity could be decreased with hypo-glucose metabolism (Kumlien et al., 1999).

Glutamatergic synaptic transduction is highly energy requiring. Cortical glucose oxidation coupled to glutamatergic synaptic activity accounts for over 80% of total glucose oxidation (Sibson et al., 1998). However, if glutamic acid-related signal transduction is depressed by repeated seizures, it could be one of the reasons for hypo-glucose metabolism in PET. The release of neurotransmitters including glutamate is enhanced by high $K^+$, a depolarizing agent (Zheng et al., 2000). The depressing of glutamate-related signal transduction in epileptogenic brain regions could cause low sensitivity of FDG uptake to high $K^+$ and the low high $K^+$/control uptake ratio. Therefore, the progression of neuronal loss including glutamatergic neuron and gliosis in the epileptogenic brain could also cause the poor response of FDG uptake to high $K^+$ and the low high $K^+$/control uptake ratio. We consider that the abnormal response to a neuro-stimulant such as high $K^+$ underlying reduced transduction and/or neuronal loss and gliosis relates to hypo-glucose metabolism in epileptogenic brain regions by PET.

The glucose transporter (Glut1) has been analyzed and quantified in brain tissues from patients undergoing surgery for seizures. Blood–brain barrier glucose transporter1 Glut1 has been suggested as up-regulated in seizures (Cornford et al., 1994). Endothelial Glut1 demonstrated increased quantities in the extravascular regions in which more EEG spiking activity had been demonstrated in interictal seizure resections (Cornford et al., 1998). These observations seem to conflict with the hypo-glucose metabolism seen in FDG-PET. However, they can be explained by the result that the FDG uptake in brain slices under the control condition showed an inverse correlation with that seen on PET. Thus the neural activity in brain slices under the control condition is less silent than that in the working brain as discussed above. In such conditions in vitro, FDG uptake could reflect Glut1 glucose transporter activity in the brain. However, FDG uptake in the epileptic brain could be defined by the response to neuro-stimulant rather than Glut1 glucose transporter activity. We speculated that the sensitivity is high under the control condition to detect the seriousness of epilepsy because it has low basement FDG uptake levels. The variance of FDG uptake in epileptic brain tissue under the high $K^+$ condition did not differ from that in the rat as a reference. This finding means that the sensitivity for the detection of epilepsy is low in FDG bioradiography under the high $K^+$ condition. The $K^+$ concentration (50 mM) in the present in vitro study might correspond to the ictal concentration in vivo as described above. This high $K^+$ concentration might be a case of low sensitivity on detection of epilepsy and poor correlation between FDG uptake in epileptic brain tissue under the high $K^+$ condition and that in PET.

In this study, FDG uptake in vitro expressed as a high $K^+$/control ratio was strongly correlated with FDG uptake in PET expressed as SG/CG and SG/CB values (Fig. 5, right). The reason is that FDG uptake in brain slices under the control condition irreversibly correlated with those in FDG-PET. To obtain the absolute values of PET data are sometimes technically difficult. In this study, we used relative values as an approximate substitute. FDG uptake in epileptogenic brain region was expressed as SG/CG and SG/CB values. FDG uptake expressed as ipsilateral to contralateral values is useful to predict outcome. Eighty six percent of TLE patients showed unilateral temporal lobe hypometabolism (UTH) and of UTH predicted a good outcome in 82% of cases. Fifty percent of patients with bitemporal hypometabolism had independent bilateral foci, and of those who proceeded to surgery only 50% had a good result (Casse et al., 2002). If we can obtain the absolute FDG uptake value in epileptogenic brain region, it would show the irreversible relation with the seriousness of epileptogenic brain. Moreover, the order of magnitude in FDG uptake in epileptogenic brain region must agree with that in the brain slices under the high $K^+$ condition. Indeed, in all seven patients who underwent excisions of epileptogenic foci and the area surrounding them identified by presurgical FDG-PET, FDG uptake in the sampled gyrus was lower than that in the contralateral gyrus and cerebellum (Table 2 and Fig. 5). FDG uptake rates in brain slices expressed as the high $K^+$/control ratio is a good indicator of the progress of epilepsy. However, it is based upon the sensitivity of morbid FDG uptake in brain slices which is high under the control condition.

Brain slices are in a sense intermediate between in vitro cell culture and in vivo studies, because the neural network and cell-to-cell communication are partially maintained in slices. In this study, the part of the brain examined in bioradiography was identical with that visualized by PET, and a comparison of in vitro with in vivo results is possible. Moreover, metabolism and physiological function in living human tissue can be compared with those in animal tissues in the same apparatus under the same conditions (Fig. 3), allowing us to evaluate the relevance of animal findings to humans.

An in vivo diagnosis based on PET, is influenced by several factors, for example, bio-degradation of the radioligand, influence of blood flow on radioligand delivery, and a limited spatial resolution (Reivich et al., 1985). Our experimental system could be useful for validating a PET-based diagnosis. In addition, various coefficients and factors, for example, the Lumped constant (Huang et al., 1980; Reivich et al., 1985), are needed for PET image processing, and their values are not always based on substantial evidence. Our system would be helpful to obtain reliable experimental values of coefficients and factors.

In order to validate diagnosis based on PET, a novel autoradiographic examination "bioradiography" was carried out in human neocortical brain slices obtained at operation from patients with intractable epilepsy who had received an FDG-PET examination preoperatively. The glucose metabolism detected in brain slices by bioradiography matched that observed by PET. Our experimental system could provide useful information for the interpretation of PET data in epileptics. It also provided a theoretical basis in performing experiments using human brain tissue that can be used to examine the pharmacological manipulation using human brain slices.

# Experimental procedures

## In vivo study

We studied seven patients (2 men and 5 women, mean age $29.3 \pm 9.5$ years) with medically intractable TLE. Patient characteristics are listed in Table 1. Magnetic resonance imaging studies were performed using a 1.5-T superconducting system with a maximal gradient capacity of 25 mT/m (Magnetom Vision; Siemens, Erlangen, Germany) and a circularly polarized head coil. PET measurements were carried out by measuring the equilibrated radioactivity 45 min after i.v. injection of FDG (150 MBq) using a PET scanner (Headtome V, Shimadzu, Kyoto, Japan). The transmission data were acquired for each patient with a rotating germanium-68 rod source for attenuation correction. The regional uptake of FDG was expressed as a standardized uptake value (SUV) (tissue activity/ml)/(injected radioisotope activity/body weight (g)). Image analysis was carried out using a medical image processing software Dr. View (Asahi Kasei Joho System Co. Ltd., Tokyo, Japan) working on a personal computer. PET data of each patient were co-registered to their own MRI using the automatic multimodality image registration (AMIR) software (Ardekani et al., 1995). Cortical

gyri sampled for brain slice study were identified on MRI and the regions of interest (ROIs) were manually placed on them. The ROIs were also placed on the cortical gyri contralateral to the sampled area and on the cerebellar cortex. The regional FDG uptake (SUV) of these ROIs was obtained from PET images co-registered to MRI. The ratios between the sampled and the SG/CG and between the SG/CB were calculated. All seven patients underwent excisions of epileptogenic foci and the surrounding neocortex with spike activity in intraoperative recordings.

## In vitro study

### Preparation of brain slices

Brain regions determined to have epileptogenecity were excised and were subjected to routine pathological examination and bioradiographical assay. For the latter, surgical specimen were rapidly transferred into oxygenated ice-cold Krebs–Ringer medium (124 mM NaCl, 5 mM KCl, 2 mM $CaCl_2$, 1 mM $MgCl_2$, 1.2 mM $KH_2PO_4$, 26 mM $NaHCO_3$ and 10 mM glucose). Then they were sectioned at 300 μm with a tissue cutter (Microslicer DTK-3000W; Dosaka EM, Kyoto, Japan) and slices were transferred into oxygenated ice-cold Krebs–Ringer medium described previously (Sasaki et al., 2002a,b). Male Wistar rats (Tokyo Jikken Dohbutsu Co. Ltd., Japan), 2 months old, were sacrificed by decapitation under light diethyl ether anesthesia. The brain was rapidly removed and placed on a tissue cutter, and coronal slices were sectioned as described above. Sectioning of all human and rat brain tissues was started within 5 min of the brain's removal. Parts of the surgical specimens were used for histopathological examination. The protocol of the human study was reviewed and approved by the Tokyo Medical and Dental University Ethics Committee (No. 110). Written informed consent was obtained from all patients after they had been told that part of the resected brain specimen would be used not for diagnostic purposes, but purely for research. All procedures on animals were in accordance with the Tokyo Metropolitan Institutes of Gerontology Guide for the Care and Use of Laboratory Animals. Human cortical brain slices were transported to our PET facility, which is located far from the operating room in Tokyo Medical and Dental University. During transportation (40 min), brain slices were preincubated with Krebs–Ringer medium and bubbled with 95% $O_2$/ 5% $CO_2$ from a portable gas cylinder, and the temperature was maintained at 34 °C with a thermostat (Sasaki and Abe, 2001). Rat brain slices were preincubated in a chamber filled with the same medium and bubbled with 95% $O_2$/5% $CO_2$ for 45 min at 34 °C.

### Bioradiographic study using FDG

FDG was synthesized by the method of Hamacher et al. (1986). The bioradiographic study was carried out using methods described previously (Sasaki et al., 2002a,b). There were two incubation conditions, control and high $K^+$. The chamber was filled with 100 ml of Krebs–Ringer medium (124 mM NaCl, 5 mM KCl, 2 mM $CaCl_2$, 1 mM $MgCl_2$, 1.2 mM $KH_2PO_4$, 26 mM $NaHCO_3$ and 10 mM glucose) as the control condition and that of high $K^+$ medium (79 mM NaCl, 50 mM KCl, 2 mM $CaCl_2$,

1 mM $MgCl_2$, 1.2 mM $KH_2PO_4$, 26 mM $NaHCO_3$ and 10 mM glucose) as the high $K^+$ condition, and placed them in the incubator at 34 °C. A continuous flow of 95% $O_2$/5% $CO_2$ gas was supplied to the medium. The brain slices were pre-incubated with Krebs–Ringer medium for the control incubation. A set of four human brain slices and of eight rat brain slices was transferred on a nylon net in the chamber and incubated with 37 MBq of FDG for 250 min. Two-dimensional images of radioactivity in the slices were recorded on a Storage Phosphor Screen through a thin polyvinylidene chloride sheet placed at the bottom of the chamber. Dynamic changes of radioactivity in the slices were measured by exposing the Storage Phosphor Screen for 10 min and changing it every 30 min. Autoradiographic images recorded on the Storage Phosphor Screen were read with a Phosphol-mager SI and analyzed with IQMac v.1.2 to obtain images. ROIs were placed on regions of gray and white matter in images of the human neocortex and the rat cerebrum. Radioactivity was expressed as "counts/pixel/10 min", which represents radioactivity per unit area per 10 min of exposure. For the quantitative analysis, the values were decay-corrected to those at the start of incubation with FDG (37 MBq). Values on the ROIs were averaged and expressed as FDG uptake (mean±SD). In each experiment, the relation between FDG uptake and time of incubation was plotted from time 0 to 250 min as in Fig. 2 and the linear relation was expressed as a slope (counts/pixel/min). The slope of the gray matter in control and high $K^+$ media, and uptake ratio between high $K^+$/control media were compared with SG/CG and SG/CB uptake ratios obtained by PET. After the dynamic autoradiographic study, the brain slices in the chamber were observed with a microscope (SZX-12-3121, Olympus Optical Co. Ltd., Tokyo, Japan) equipped with a digital camera (Coolpix 100, Nikon Co., Ltd., Tokyo, Japan) and photographed for anatomical identification.

## Statistical analysis

The bioradiographic uptake in gray matter was expressed as the rate of uptake per pixel per minute (counts/pixel/min) in control medium and that in high $K^+$ medium and the uptake ratio between high $K^+$/control media. The values were expressed as the mean±SD for 7 patients and 6 rats. The homoscedasticity in the uptake rate and the uptake ratio between rat and human tissues was analyzed with the F test. Statistical significance was determined using the Wilcoxon/Kruskal–Wallis test for differences of data with an outlier (arrow in Fig. 4) and without an outlier.

The magnitude of the relationship between FDG-PET and FDG bioradiographic data with an outlier (7 patients) and without an outlier (6 patients) was determined by a regression analysis. The statistical significance of the correlation was calculated using an F test.

## Acknowledgment

## REFERENCES

Ardekani, B.A., Braun, M., Hutton, B.F., Kanno, I., Iida, H., 1995. A fully automatic multimodality image registration algorithm. J. Comput. Assist. Tomogr. 19, 615–623.

Cascino, G.D., 2004. Surgical treatment for extratemporal epilepsy. Curr. Treat. Options Neurol. 6, 257–262.

Casse, R., Rowe, C.C., Newton, M., Berlangieri, S.U., Scott, A.M., 2002. Positron emission tomography and epilepsy. Mol. Imaging Biol. 4, 338–351.

Cohen-Gadol, A.A., Wilhelmi, B.G., Collignon, F., White, J.B., Britton, J.W., Cambier, D.M., Christianson, T.J., Marsh, W.R., Meyer, F.B., Cascino, G.D., 2006. Long-term outcome of epilepsy surgery among 399 patients with nonlesional seizure foci including mesial temporal lobe sclerosis. J. Neurosurg. 104, 513–524.

Cornford, E.M., Hyman, S., Swartz, B.E., 1994. The human brain GLUT1 glucose transporter: ultrastructural localization to the blood–brain barrier endothelia. J. Cereb. Blood Flow Metab. 14, 106–112.

Cornford, E.M., Hyman, S., Cornford, M.E., Landaw, E.M., Delgado-Escueta, A.V., 1998. Interictal seizure resections show two configurations of endothelial Glut1 glucose transporter in the human blood–brain barrier. J. Cereb. Blood Flow Metab. 18, 26–42.

Debets, R.M., Sadzot, B., van Isselt, J.W., Brekelmans, G.J., Meiners, L.C., van Huffelen, A.O., Franck, G., van Veelen, C.W., 1997. Is $^{11}$C-flumazenil PET superior to $^{18}$FDG PET and $^{123}$I-iomazenil SPECT in presurgical evaluation of temporal lobe epilepsy? J. Neurol., Neurosurg. Psychiatry 62, 141–150.

During, M.J., Spencer, D.D., 1993. Extracellular hippocampal glutamate and spontaneous seizure in the conscious human brain. Lancet 341, 1607–1610.

Fazekas, F., Kapeller, P., Schmidt, R., Stollberger, R., Varosanec, S., Offenbacher, H., Fazekas, G., Lechner, H., 1995. Magnetic resonance imaging and spectroscopy findings after focal status epilepticus. Epilepsia 36, 946–949.

Graham, D.I., Lantos, P.L., 2002. Greenfield's Neuropathology, 7th ed. Arnold, London.

Hamacher, K., Coenen, H.H., Stocklin, G., 1986. Efficient stereospecific synthesis of no-carrier-added 2-[$^{18}$F]-fluoro-2-deoxy-D-glucose using aminopolyether supported nucleophilic substitution. J. Nucl. Med. 27, 235–238.

Honegger, P., Pardo, B., 1999. Separate neuronal and glial $Na^+$, $K^+$-ATPase isoforms regulate glucose utilization in response to membrane depolarization and elevated extracellular potassium. J. Cereb. Blood Flow Metab. 19, 1051–1059.

Huang, S.C., Phelps, M.E., Hoffman, E.J., Sideris, K., Selin, C.J., Kuhl, D.E., 1980. Noninvasive determination of local cerebral metabolic rate of glucose in man. Am. J. Physiol. 238, E69–E82.

Kumlien, E., Hartvig, P., Valind, S., Oye, I., Tedroff, J., Langstrom, B., 1999. NMDA-receptor activity visualized with (S)-[N-methyl-$^{11}$C]ketamine and positron emission tomography in patients with medial temporal lobe epilepsy. Epilepsia 40, 30–37.

Matheja, P., Weckesser, M., Debus, O., Lottgen, J., Schuierer, G., Schober, O., Kurlemann, G., 2000. Drug-induced changes in cerebral glucose consumption in bifrontal epilepsy. Epilepsia 41, 588–593.

Mtsumura, K., Bergstrom, M., Onoe, H., Takechi, H., Westerberg, G., Antoni, G., Bjurling, P., Jacobson, G.B., Langstrom, B., Watanabe, Y., 1995. In vitro positron emission tomography (PET): use of positron emission tracers in functional imaging in living brain slices. Neurosci. Res. 22, 219–229.

McGeer, P.L., Kamo, H., Harrop, R., McGeer, E.G., Martin, W.R., Pate, B.D., Li, D.K., 1986. Comparison of PET, MRI, and CT with pathology in a proven case of Alzheimer's disease. Neurology 36, 1569–1574.

Meldrum, B.S., 2000. Glutamate as a neurotransmitter in the brain: review of physiology and pathology. J. Nutr. 130 (4S Suppl.), 1007S–1015S.

Minoshima, S., Cross, D.J., Foster, N.L., Henry, T.R., Kuhl, D.E., 1999. Discordance between traditional pathologic and energy metabolic changes in very early Alzheimer's disease. Pathophysiological implications. Ann. N. Y. Acad. Sci. 893, 350–352.

Murata, T., Matsumura, K., Onoe, H., Bergstrom, M., Takechi, H., Sihver, S., Sihver, W., Neu, H., Andersson, Y., Ogren, M., Fasth, K.J., Langstrom, B., Watanabe, Y., 1996. Receptor imaging technique with $^{11}$C-labeled receptor ligands in living brain slices: its application to time-resolved imaging and saturation analysis of benzodiazepine receptor using [$^{11}$C]Ro15-1788. Neurosci. Res. 25, 145–154.

Petroff, O.A., Errante, L.D., Rothman, D.L., Kim, J.H., Spencer, D.D., 2002. Glutamate–glutamine cycling in the epileptic human hippocampus. Epilepsia 43, 703–710.

Pfund, Z., Chugani, D.C., Juhasz, C., Muzik, O., Chugani, H.T., Wilds, I.B., Seraji-Bozorgzad, N., Moore, G.J., 2000. Evidence for coupling between glucose metabolism and glutamate cycling using FDG PET and 1H magnetic resonance spectroscopy in patients with epilepsy. J. Cereb. Blood Flow Metab. 20, 871–878.

Reivich, M., Alavi, A., Wolf, A., Fowler, J., Russell, J., Arnett, C., MacGregor, R.R., Shiue, C.Y., Atkins, H., Anand, A., Dann, R., Greenberg, J.H., 1985. Glucose metabolic rate kinetic model parameter determination in humans: the lumped constants and rate constants for [$^{18}$F]fluorodeoxyglucose and [$^{11}$C] deoxyglucose. J. Cereb. Blood Flow Metab. 5, 179–192.

Sasaki, T., Abe, K., 2001. Development of a transportable incubator for autoradiographic experiments with positron emitter-labeled tracers in living brain tissues. Brain Res. Brain Res. Protoc. 8, 170–175.

Sasaki, T., Ishiwata, K., Murata, T., Senda, M., 2002a. Demonstration of competition between endogenous dopamine and [$^{11}$C]raclopride binding in in vitro brain slices using a dynamic autoradiography technique. Synapse 44, 42–50.

Sasaki, T., Kawamura, K., Tanaka, Y., Ando, S., Senda, M., 2002b. Assessment of choline uptake for the synthesis and release of acetylcholine in brain slices by a dynamic autoradiographic technique using [$^{11}$C]choline. Brain Res. Brain Res. Protoc. 10, 1–11.

Sibson, N.R., Shen, J., Mason, G.F., Rothman, D.L., Behar, K.L., Shulman, R.G., 1998. Functional energy metabolism: in vivo $^{13}$C-NMR spectroscopy evidence for coupling of cerebral glucose consumption and glutamatergic neuronal activity. Dev. Neurosci. 20, 321–330.

Sokoloff, L., 1999. Energetics of functional activation in neural tissues. Neurochem. Res. 24, 321–329.

Sokoloff, L., Takahashi, S., Gotoh, J., Driscoll, B.F., Law, M.J., 1996. Contribution of astroglia to functionally activated energy metabolism. Dev. Neurosci. 18, 344–352.

Somjen, G.G., 1975. Electrophysiology of neuroglia. Annu. Rev. Physiol. 37, 163–190.

Takahashi, S., Driscoll, B.F., Law, M.J., Sokoloff, L., 1995. Role of sodium and potassium ions in regulation of glucose metabolism in cultured astroglia. Proc. Natl. Acad. Sci. U. S. A. 92, 4616–4620.

Velisek, L., Moshe, S.L., 2003. Temporal lobe epileptogenesis and epilepsy in the developing brain: bridging the gap between the laboratory and the clinic. Epilepsia 44, 51–59.

Zheng, L., Godfrey, D.A., Waller, H.J., Godfrey, T.G., Chen, K., Sun, Y., 2000. Effects of high-potassium-induced depolarization on amino acid chemistry of the dorsal cochlear nucleus in rat brain slices. Neurochem. Res. 25, 823–835.

# Neural correlates of regional EEG power change

N. Oishi,[a] T. Mima,[a,d,*] K. Ishii,[b,d] K.O. Bushara,[c,d] T. Hiraoka,[e] Y. Ueki,[a] H. Fukuyama,[a] and M. Hallett[d]

[a]Human Brain Research Center, Kyoto University Graduate School of Medicine, Kyoto 606-8507, Japan
[b]Positron Medical Center, Tokyo Metropolitan Institute of Gerontology, 35-2 Sakaecho, Itabashi, Tokyo 173-0015, Japan
[c]Neurology service, Rm 4B135, Minneapolis Veterans Affairs Medical Center, One Veterans Drive, Minneapolis, MN 55417, USA
[d]NINDS, National Institutes of Health, Bethesda, MD 20892, USA
[e]Department of Radiology, Kyoto City hospital, Mibu-takadahigasi-cho, Nakagyo-ku, Kyoto 604-8845, Japan

To clarify the physiological significance of task-related change of the regional electroencephalogram (EEG) rhythm, we quantitatively evaluated the correlation between regional cerebral blood flow (rCBF) and EEG power. Eight subjects underwent $H_2^{15}O$ positron emission tomography scans simultaneously with EEG recording during the following tasks: rest condition with eyes closed and open, self-paced movements of the right and left thumb and right ankle. EEG signals were recorded from the occipital and bilateral sensorimotor areas. Cortical activation associated with EEG rhythm generation was studied by the correlation between rCBF and EEG power. There were significant negative correlations between the sensorimotor EEG rhythm at 10–20 Hz on each side and the ipsilateral sensorimotor rCBF and between the occipital EEG rhythm at 10–20 Hz and the occipital rCBF. The occipital EEG rhythm showed a positive correlation with the bilateral medial prefrontal rCBF, while the right sensorimotor EEG rhythm showed a positive correlation with the left prefrontal rCBF. In conclusion, decrease in the regional EEG rhythm at 10–20 Hz might represent the neuronal activation of the cortex underlying the electrodes, at least for the visual and sensorimotor areas. The neural network including the prefrontal cortex could play an important role to generate the EEG rhythm.
© 2007 Elsevier Inc. All rights reserved.

Keywords: Neural networks; Positron emission tomography (PET); Regional cerebral blood flow; Sensorimotor; Visual

---

Abbreviations: ANCOVA, analysis of covariance; EEG, electroencephalogram; EMG, electromyogram; EOG, electro-oculogram; ERD, event-related desynchronization; ERS, event-related synchronization; FWHM, full width at half-maximum; M1, primary motor cortex; PET, positron emission tomography; rCBF, regional cerebral blood flow; S1, primary sensory cortex; SM1, primary sensorimotor cortex; SPM, statistical parametric map.
* Corresponding author. Human Brain Research Center, Kyoto University Graduate School of Medicine, 54 Kawahara-cho, Shogoin, Sakyo-ku, Kyoto 606-8507, Japan. Fax: +81 75 751 3202.
E-mail address: mima@kuhp.kyoto-u.ac.jp (T. Mima).
Available online on ScienceDirect (www.sciencedirect.com).

## Introduction

The electroencephalogram (EEG) represents the summed postsynaptic potentials of cortical neurons (Niedermeyer and Lopes da Silva. 1987). The generator mechanisms of EEG rhythm in various frequency bands, however, are not well understood.

In normal subjects, the EEG rhythm at 8–12 Hz is usually most conspicuous over the parieto-occipital area (Berger. 1929; Pfurtscheller and Lopes da Silva, 1999) and is called the occipital alpha band rhythm. The EEG alpha band rhythm may be associated with the alert and yet relaxed state and is commonly used as an indirect measure of the functional organization of brain. It is well known that normal awake alpha band rhythms are 'blocked' (substantially reduced in amplitude) by eye opening and moderate to difficult mental tasks (Berger. 1930. 1932; Nunez et al., 2001; Vijn et al., 1991). Thus, some authors suggested that the occipital alpha band rhythm might be considered as an idling rhythm of visual areas (Kuhlman. 1978).

One of the most relevant activities overlapping the occipital alpha band rhythm is the so-called mu rhythm which is restricted over the hand area of the primary sensorimotor cortex (SM1) and is suppressed not by eye opening but by active hand movements. The sensorimotor mu rhythm could also be considered as an idling rhythm of sensorimotor areas (Kuhlman, 1978; Pfurtscheller. 1992). Although the role of the thalamocortical circuitry in the generation of sleep spindles has been emphasized (Steriade et al., 1990), the neurophysiological mechanisms by which the regional alpha band rhythm such as the occipital alpha or the sensorimotor mu rhythm are to be generated or suppressed are still unclear.

Higher frequency EEG waves such as the beta band rhythm (13–30 Hz) are associated with the cortical activation most pronounced during the awake state and rapid eye movement sleep (Nofzinger et al., 2000). During various motor tasks, EEG studies showed a transient decrease of EEG power in the beta band (Pfurtscheller. 1989), which is called event-related desynchronization (ERD) (Pfurtscheller. 1977; Pfurtscheller and Aranibar. 1977)

or task-related power decrease (Gerloff et al., 1998). This decrease starts 1–2 s prior to the movement onset and is followed by a rebound-like increase just after termination of the movement (event-related synchronization: ERS) (Pfurtscheller, 1992). It is speculated that the motor cortex shifts from an activated state during preparation and execution of movement (working cortex) to a resting state after termination of movement or, in other words, from a processing mode to an 'idling' mode (Pfurtscheller et al., 1996). This hypothesis is also supported by a transcranial magnetic stimulation study showing decreased corticospinal excitability at the time of the 20-Hz event-related synchronization (Chen et al., 1998). However, the generator mechanism of regional beta band rhythm is still unknown.

Brain electrical activity represents the single greatest demand on cerebral metabolism (Erecinska and Silver, 1989), suggesting that measurement of electrical energy also should be coupled to cerebral metabolism and perfusion. In normal subjects, cerebral glucose uptake and blood flow are generally accepted as tightly coupled measures of cerebral energy utilization (Sokoloff, 1977, 1981). The association between EEG power and cerebral glucose metabolism has been occasionally studied using the 18-fluoro-deoxyglucose positron emission tomography (PET) technique (Larson et al., 1998; Oakes et al., 2004; Schreckenberger et al., 2004). However, a limitation of the 18-fluoro-deoxyglucose tracer is that over the span of 30 min it is difficult to ensure that the subject remains in the same functional state (Oakes et al., 2004). Regional cerebral blood flow (rCBF) has been used as an indirect measure of functional neural activity (Raichle, 1987) and the PET technique is considered to be the 'gold standard' in CBF measurements in humans (Feng et al., 2004). Measurement of rCBF using $H_2^{15}O$ PET has been well established based on the single-tissue compartment model for diffusible tracers in at least physiologically normal brain tissue (Sadato et al., 1998). The $H_2^{15}O$ tracer has shorter time frame (10–30 s) than the 18-fluoro-deoxyglucose tracer (20–30 min) and the results of $H_2^{15}O$ PET examinations directly depend on the acute cerebral state of activation during tracer injection (Schreckenberger et al., 2004). In normal subjects, cerebral blood flow is generally accepted as tightly coupled measures of cerebral energy utilization (Sokoloff, 1977, 1981). It was reported that EEG power showed strong associations with rCBF in most frequency bands including the alpha and beta range (Leuchter et al., 1999). Therefore, taken together with the EEG power change described above, it is predicted that rCBF associated with the neuronal activation might covary with the EEG power in at least normal subjects. Although previous reports (Ingvar et al., 1976; Paulson and Sharbrough, 1974) mentioned the relationship between EEG and rCBF in humans, the record of EEG and rCBF could not be done simultaneously due to limitations in the EEG and rCBF technique. Recently, the association between EEG power and rCBF recorded simultaneously has been occasionally studied using the $H_2^{15}O$ technique (Leuchter et al., 1999; Nakamura et al., 1999; Sadato et al., 1998). However, the previous reports investigated a correlation between rCBF and the EEG rhythm averaged across the whole scalp. The averaged EEG rhythm might be inappropriate to investigate regional EEG power change such as sensorimotor mu rhythm because the occipital alpha band rhythm may diminish an effect of sensorimotor mu rhythm in the averaged alpha power. Therefore, it would be preferable to investigate the relationship between rCBF change induced by several tasks and the regional EEG rhythm to clarify

neurophysiological mechanisms in the generation or suppression of the regional EEG power. To achieve this goal, we employed rather simple tasks that are commonly used in clinical EEG recording.

The purpose of the present study is to quantitatively evaluate the correlation between rCBF changes using $H_2^{15}O$ PET and EEG power changes induced by several motor tasks and clarify what brain regions are involved in the generation and suppression of the regional EEG rhythms.

## Methods

### Subjects

Eight right-handed healthy volunteers (5 males and 3 females; mean age±SD, 42±10 years) participated in the experiment. The protocol was approved by the NINDS Institutional Review Board and the NIH Radiation Safety Committee. All subjects gave their written informed consent for the study and had no medical history of neurological or psychiatric disorders.

### Tasks

The subjects lay in a supine position and the following tasks were performed twice for each (total 10 times):

1. rest condition with eyes closed (EC)
2. rest condition with eyes open (EO)
3. self-paced right thumb abduction and adduction movement (1–2 Hz) with eyes closed (RH)
4. self-paced left thumb abduction and adduction movement (1–2 Hz) with eyes closed (LH)
5. self-paced right ankle extension and flexion movement (1–2 Hz) with eyes closed (RF)

The order of tasks was randomized across subjects. Electrophysiological recording and PET scanning were carried out simultaneously in all conditions (Fig. 1).

### Electrophysiological recording

EEG signals were recorded from 6 electrodes (O1, O2, C3, C4, FC3, FC4 according to the International 10–20 System) secured with collodion and referenced to the right earlobe electrode (A2). The left earlobe electrode (A1) was recorded as a separate channel. To reliably estimate the scalp EEG potential, we converted the EEG signals into the digitally linked earlobe reference before further analysis (Mima and Hallett, 1999; Nunez et al., 1997). A previous study showed that the electrode locations of FC3/C3, FC4/C4 and O1/O2 are just over the left and right SM1 and the occipital cortex, respectively (Steinmetz et al., 1989). Electromyogram (EMG) signals were recorded from 5 muscles (right abductor pollicis brevis [APB], biceps [BIC], left APB, BIC and right hamstring). To monitor the eye movement and blinking, electro-oculograms (EOGs) were monitored by pairs of electrodes placed at the left and right lateral canthus for horizontal eye movement and by another pair of electrodes placed below and above the right eye for vertical eye movement. To monitor tongue movement, a surface electrode placed at the upper edge of the right nasolabial fold